Receptivity, instability and breakdown of Görtler flow

LARS-UVE SCHRADER[1], LUCA BRANDT[1] AND TAMER A. ZAKI[2]†

[1]Linné Flow Centre, KTH Mechanics, SE-100 44 Stockholm, Sweden

[2]Department of Mechanical Engineering, Imperial College London, London SW7 2AZ, UK

Receptivity, disturbance growth and breakdown to turbulence in Görtler flow are studied by spatial direct numerical simulation (DNS). The boundary layer is exposed to free-stream vortical modes and localized wall roughness. We propose a normalization of the roughness-induced receptivity coefficient by the square root of the Görtler number. This scaling removes the dependence of the receptivity coefficient on wall curvature. It is found that vortical modes are more efficient at generating Görtler vortices than localized roughness. The boundary layer is most receptive to zero- and low-frequency free-stream vortices, exciting steady and slowly travelling Görtler modes. The associated receptivity mechanism is linear and involves the generation of boundary-layer streaks, which soon evolve into unstable Görtler vortices. This connection between transient and exponential amplification is absent on flat plates and promotes transition to turbulence on curved walls. We demonstrate that the Görtler boundary layer is also receptive to high-frequency free-stream vorticity, which triggers steady Görtler rolls via a nonlinear receptivity mechanism. In addition to the receptivity study, we have carried out DNS of boundary-layer transition due to broadband free-stream turbulence with different intensities and frequency spectra. It is found that nonlinear receptivity dominates over the linear mechanism unless the free-stream fluctuations are concentrated in the low-frequency range. In the latter case, transition is accelerated due to the presence of travelling Görtler modes.

Key words: boundary layer receptivity, transition to turbulence

1. Introduction

Flow over walls with concave curvature is studied using direct numerical simulation (DNS). As compared with flow over a flat plate, the wall-normal balance of forces on the fluid is modified by the presence of a centrifugal force, which increases away from the wall and is balanced mainly by the pressure force. A sudden wall-normal displacement of fluid inside the boundary layer, e.g. due to surface roughness, may destroy this balance and destabilize the shear layer. This instability mechanism may cause laminar boundary layers to transition to turbulence and is relevant e.g. on the lower side of a turbine blade.

† Email address for correspondence: t.zaki@imperial.ac.uk

1.1. *Linear instability*

The pioneering work for boundary layers on constant-curvature concave walls was carried out by Görtler (1941), whose name became associated with this type of flow, the instability and the governing stability parameter. Floryan (1991) and Saric (1994) provided comprehensive reviews of the experimental, theoretical and numerical studies reported since Görtler's work. Experimental evidence (e.g. Ito 1980) suggests that the boundary-layer instability appears as streamwise-aligned counter-rotating steady vortices with constant spanwise wavelength, referred to as Görtler rolls. These rolls are accompanied by energetic longitudinal high- and low-momentum streaks caused by the vertical displacement of fluid by the vortices. The streamwise length scale of the disturbance mode is thus of the same order as that of the underlying basic state. Therefore, the concepts of parallel flow and local normal modes do not apply in Görtler boundary layers. This is reflected by the linearized stability equations given by Floryan & Saric (1982), where terms involving the wall-normal velocity and the streamwise derivatives of the basic state are retained. Indeed, attempts to determine a neutral-stability curve by classic stability theory were not successful. The reason for this failure was for the first time explained by Hall (1983), who instead suggested a streamwise-marching numerical procedure to solve the parabolic stability equations. However, Hall (1983) was likewise unable to locate the first point of neutral stability, realizing that the evolution of the Görtler rolls depends on the shape and the streamwise location of the spatial initial conditions. He concluded that the concept of neutral stability is not meaningful in Görtler boundary layers except in the small-wavelength asymptotic limit (Hall 1982). Lee & Liu (1992) later revised this view, pointing out that the initial disturbances of Hall (1983) were not consistent with the governing hydrodynamic equations and thus underwent some transient adjustment before developing into a Görtler mode. Bottaro & Luchini (1999) resurrected local stability theory in Görtler flows, comparing modal amplification rates from local analysis of different complexity with those from marching solutions. They found that even the simplest local model – the original analysis by Görtler (1941) – is satisfactory above a local Görtler number of seven (based on the Blasius length). Below this value (farther upstream), the evolution of the Görtler modes is dependent on their excitation (receptivity), which hampers the identification of a unique critical Görtler number.

1.2. *Receptivity*

Receptivity initiates the process of laminar–turbulent boundary-layer transition. External perturbations may intrude into the shear layer via its boundaries – the wall and the boundary-layer edge. Sources of such perturbations are e.g. wall roughness and free-stream turbulence. Energy is transferred from these sources to the boundary layer, where Görtler instability modes may be excited via different mechanisms. A review of the receptivity problem is given by Bassom & Seddougui (1995). Denier, Hall & Seddougui (1991) reported that the excitation of instability modes by wall roughness is most efficient for roughnesses with a spanwise length scale comparable to the boundary-layer thickness. Streamwise-distributed roughness was found to be more relevant than localized roughness. Bertolotti (1993) demonstrated that streamwise-aligned riblets efficiently excite Görtler rolls. Receptivity to free-stream vortical disturbances at the leading edge was discussed in the review by Hall (1990). Bippes & Deyhle (1992) observed in wind-tunnel experiments that Görtler rolls can easily be excited by free-stream disturbances originating from the screens in the settling chamber. Luchini & Bottaro (1998) computed for different external perturbations Green's functions based on the eigenmodes of the adjoint parabolic

stability equations. Multiplying these Green's functions with the external disturbances yielded the downstream amplitude of the centrifugal instability. Roughness receptivity was found to be most efficient at the leading edge for disturbances with zero streamwise wavenumber and $O(1)$ spanwise wavenumber. Maximum receptivity to free-stream vorticity was observed for the spanwise wavenumber of the most unstable Görtler mode. Based on the linear stability operator ('spatial propagator'), Cossu *et al.* (2000) computed optimal inflow perturbations in curved boundary layers. The propagator was reconstructed from different sets of inlet conditions and streamwise-marching solutions. The wall-normal profiles of the optimal inflow conditions were found to reach from the shear region far out into the free stream, suggesting efficient boundary-layer receptivity to free-stream disturbances.

1.3. *Secondary instability and breakdown*

Peerhossaini & Wesfreid (1988) studied the flow through a curved straight water channel. Their dye visualizations show that low- and high-momentum streaks generated by Görtler vortices distort the flow profiles such that the low-momentum regions take characteristic, mushroom-like shapes. At this stage the primary vortex-streak system starts to oscillate, indicating the onset of secondary instability. The paper by Swearingen & Blackwelder (1987) is often considered the most important contribution to the clarification of secondary instability and breakdown of longitudinal vortices. Swearingen & Blackwelder (1987) observed in a wind-tunnel experiment with a large-radius concave test section that the Görtler rolls and streaks become wavy before they break down individually (see also Bippes 1972). Two forms of waviness with different symmetries about the primary vortex axis were identified. These modes, nowadays known as sinuous and varicose secondary instabilities, appear near the spanwise and wall-normal inflection points of the distorted streamwise mean profiles, respectively. The sinuous type was found to occur more frequently than the varicose type. Liu & Domaradzki (1993) reproduced these results by temporal DNS with a pseudo-spectral method. Yu & Liu (1994) analysed the kinetic energy balance of secondary instability and demonstrated for the configuration of Swearingen & Blackwelder (1987) that the growth rate of the sinuous mode is larger than that of the varicose mode. Park & Huerre (1995) confirmed in a curved asymptotic-suction boundary layer the earlier amplification of sinuous instabilities. However, according to Li & Malik (1995) the competition between sinuous and varicose modes depends on the spanwise wavenumber of the underlying Görtler vortex. It turned out that long-wavelength vortices tend to develop varicose horseshoe structures rather than sinuous oscillations. Lee & Liu (1992) computed the nonlinear development of Görtler vortices and the spatial variations of skin friction. Girgis & Liu (2006) reported that the skin-friction coefficient in transitional and turbulent Görtler boundary layers rises well beyond the level of turbulent flat-plate boundary layers. They attributed this behaviour to a nonlinear modification of the primary steady flow by wavy secondary instabilities. The strong rise in skin friction was also observed in experiments (Schultz & Volino 2003; Tandiono, Winoto & Shah 2009).

   DNS studies of Görtler flow have so far considered the temporal framework of the physical problem, whereas spatial DNS of streamwise developing Görtler boundary layers (the most appropriate approach) is lacking to our knowledge. This motivates the present paper. We report spatial DNS of the flow over concave walls with three different radii of curvature, of which one matches the wall curvature in the experiments by Tandiono, Winoto & Shah (2008) and Tandiono *et al.* (2009). The simulations presented herein are the first spatial DNS of the receptivity to free-stream turbulence
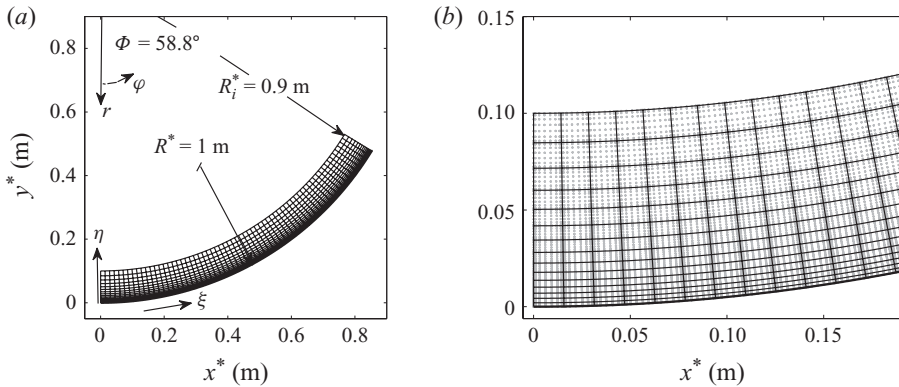
FIGURE 1. Concave plate, radius of curvature $R^* = 1$ m. (*a*) Computational domain (grid A, table 1). (*b*) Numerical grid near the inflow plane. Spectral elements (black) and Gauss–Lobatto–Legendre nodes (grey dots).

and the subsequent laminar–turbulent transition of the Görtler boundary layer. Such spatial DNS have so far only been reported for flat-plate flow (Jacobs & Durbin 2001; Brandt, Schlatter & Henningson 2004), but not for Görtler boundary layers. We demonstrate that the receptivity to vortical free-stream disturbances can be linear or nonlinear, considering both single vortical modes (§ 2) and free-stream turbulence (§ 3). An alternative source of receptivity – localized wall roughness – is also studied in § 2. The importance of roughness as a Görtler vortex generator is compared with that of free-stream vorticity.

2. Receptivity and growth

2.1. *Spectral element code and domain*

The spectral element method (SEM; Patera 1984) provides spectral accuracy in space for geometries beyond the scope of global spectral methods using Fourier series. The SEM is thus ideally suited for meshing curved surfaces with wall roughness. The simulation code used was developed by Fischer *et al.* (2008). It allows solving both the full nonlinear and the linearized Navier–Stokes equations. The physical domain is decomposed into spectral elements. The solution to the governing equations is approximated locally on these elements as a sum of orthogonal basis functions (Legendre polynomials). The expansion of the flow variables, the spatial discretization and the time-integration scheme are briefly summarized in Schrader *et al.* (2010), where additional references to the SEM implementation are given. The convergence of the spatial approximation is $\propto e^{-N}$, where the spectral accuracy is determined by the highest-order Legendre polynomial ($N = 7$ here). Figure 1(*b*) depicts the Gauss–Lobatto–Legendre grid used for the computation of the velocity field. The pressure is computed on a staggered grid with spectral order $N - 2$ (Gauss–Legendre grid). Table 1 lists the SEM grids used. The domain size is given in cylindrical coordinates, with R^* determining the radius of curvature, Φ the arc length and L_z^* the span of the plate (cf. figure 1*a*). When presenting the results we will follow convention and use the tangential, normal and spanwise plate coordinates ξ, η and z instead. The computational domain shown in figure 1(*a*) covers about 60 % of the wind-tunnel test section of Tandiono *et al.* (2008) with a radius of wall curvature of 1 m. The

Grid	(R^*, R_i^*) (m)	Φ(deg.)	$L_z^*(\times 10^{-2})$ (m)	$n_\xi \times n_\eta \times n_z$	N	N_{tot} ($\times 10^6$)
A	(1.0,0.9)	58.5	0.74–4.46	$65 \times 15 \times 3$	7	1.063
B	(1.0,0.9)	67.5	0.74–4.46	$75 \times 15 \times 3$	7	1.227
C	(1.0,0.9)	67.5	2.55	$75 \times 15 \times 5$	7	2.007
D	(2.0,1.9)	29.3	1.27	$65 \times 15 \times 3$	7	1.063
E	(2.0,1.9)	33.8	1.27	$75 \times 15 \times 3$	7	1.227
F	(4.0,3.9)	14.6	1.27	$65 \times 15 \times 3$	7	1.063
G	(4.0,3.9)	16.9	1.27	$75 \times 15 \times 3$	7	1.227

TABLE 1. Parameters of the SEM grids. R^*, R_i^* and Φ as in figure 1(a); the star denotes dimensional quantities. n_ξ, n_η and n_z are the numbers of elements in the tangential, wall-normal and spanwise directions; N is the highest order of the polynomial basis functions and $N_{tot} = (n_\xi N + 1)(n_\eta N + 1)(n_z N + 1)$ is the total number of Gauss–Lobatto–Legendre points.

meshes denoted by A, B and C are used for this configuration, while grids D–G denote simulations of flow over plates with larger radii.

2.2. Base flow

The velocity field $U = U_b + u$ is decomposed into a steady, spanwise-independent base flow U_b and a disturbance u, where u can be unsteady or steady three-dimensional. Since the base flow is invariant in the spanwise direction, it has been computed on two-dimensional SEM meshes. The tangential and normal grid resolutions of these meshes are identical to those of the three-dimensional grids in table 1. The base-flow fields serve both as initial conditions for nonlinear Navier–Stokes computations and as basic states for solutions to the linearized disturbance equations. Zero-slip conditions are prescribed at the wall, and Blasius profiles are specified at the inlet and the top boundary. The inflow is at Reynolds number $Re_{\delta_0^\star} \equiv U_\infty \delta_0^\star/\nu = 198.36$, where U_∞ is the free-stream velocity, $\delta_0^\star$ is the displacement thickness of the inflow profile and ν is the kinematic viscosity. Zero-stress conditions along with a constant pressure are applied at the outlet. This outflow is inconsistent with the upstream flow field, where the pressure varies in the wall-normal direction owing to the centrifugal force. Therefore, the outlet is located far downstream ($\Phi_{2D} = 135°$, $n_{\xi 2D} = 150$ elements) to avoid any influence of the outflow conditions on the region of interest. The reference velocity is given by U_∞ and the reference length by $\delta_0^\star$. Görtler flows also feature a large characteristic length scale, the radius of wall curvature R. Here, three values of R are considered. These correspond to dimensional radii (marked by a star) of $R^* = 1$, 2 and 4 m based on the experimental parameters of Tandiono et al. (2008; 'case 1', $U_\infty^* = 2.85 \text{ m s}^{-1}$). In the reference system adopted, these values become $R = 957.85$, 1915.71 and 3831.42, respectively. When presenting the results we shall call the three cases as $R^* = 1$ m, $R^* = 2$ m and $R^* = 4$ m for brevity. The radius R also enters the stability parameter of Görtler boundary layers, the Görtler number

$$G_\theta \equiv \frac{U_\infty \theta}{\nu} \sqrt{\frac{\theta}{R}} = Re_\theta \sqrt{\frac{\theta}{R}}. \tag{2.1}$$

Note that G_θ is usually based on the boundary-layer momentum-loss thickness θ. It represents a combination of the Reynolds number and a curvature parameter, thus relating the destabilizing inertial and centrifugal forces to the stabilizing viscous force.
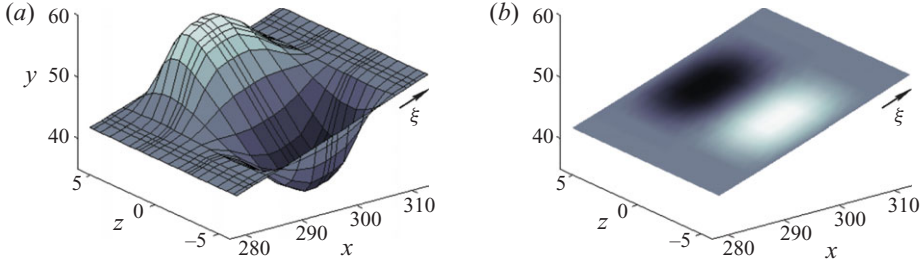
FIGURE 2. (Colour online available at journals.cambridge.org/FLM) (*a*) Surface-roughness function $h(\xi, z)$ with $\beta = 0.546$ ($\Lambda = 250$), $\xi_r = 300.9$ and $\xi_{rise} = \xi_{fall} = 15.05$. The height, $\varepsilon_r = 0.01\delta_r^\star$, is enlarged by a factor of 500 in the figure. (*b*) Inhomogeneous boundary conditions for the streamwise disturbance velocity u as a model for the roughness shown in (*a*); white/black: $u = \pm 6 \times 10^{-3}$.

2.3. *Perturbation*

Nonlinear and linear Navier–Stokes computations were performed. The computational grids for the nonlinear simulations (B, C, E and G) accommodate a sponge region at the downstream end of the domain, where the base-flow profiles are enforced by a volume force $\boldsymbol{F} = \lambda(\xi)(\boldsymbol{U}_b - \boldsymbol{U})$. The function $\lambda(\xi)$ varies smoothly between zero and $\lambda_{max} = 0.8$ inside the sponge while vanishing everywhere else (see also Chevalier *et al.* 2007). This ensures a disturbance-free outflow without affecting the upstream flow field. It turned out that no sponge was needed for the linear simulations; therefore, the corresponding meshes (A, D and F) are about 15 % shorter. On the upper boundary, zero-disturbance conditions are prescribed, justified as long as the top boundary is far enough away from the wall (nearly eight outflow boundary-layer thicknesses here). Periodic conditions are enforced in the spanwise direction. Thus, the domain width sets the fundamental spanwise disturbance wavelength λ_z, normalized here as

$$\Lambda \equiv \frac{U_\infty \lambda_z}{\nu} \sqrt{\frac{\lambda_z}{R}}. \tag{2.2}$$

Note that Λ assumes a similar form as the Görtler number in (2.1). The perturbations are generated as inflow conditions or wall boundary conditions, as discussed next.

2.3.1. *Surface roughness*

Streamwise-localized, spanwise-sinusoidal roughness elements of the form

$$h(\xi, z) = \varepsilon_r \left[S\left(\frac{\xi - \xi_{start}}{\Delta\xi_{rise}} \right) - S\left(\frac{\xi - \xi_{end}}{\Delta\xi_{fall}} + 1 \right) \right] \sin\left(2\pi z/\lambda_z \right) \tag{2.3}$$

are considered (figure 2*a*). The roughness bump is characterized by its height ε_r, spanwise width λ_z and streamwise extent $\xi \in [\xi_{start}, \xi_{end}]$, where ξ_{start} and ξ_{end} define the bump length $\Delta\xi_r \equiv \xi_{end} - \xi_{start}$ and the nominal location $\xi_r \equiv 0.5(\xi_{start} + \xi_{end})$. The streamwise shape is given by the smooth step function S with rising and falling flanks $\Delta\xi_{rise}$ and $\Delta\xi_{fall}$. The function S is

$$S(\bar{\bar{\xi}}) = \begin{cases} 0, & \bar{\bar{\xi}} \leqslant 0, \\ 1/(1 + e^{(1/(\bar{\bar{\xi}}-1)+1/\bar{\bar{\xi}})}), & 0 < \bar{\bar{\xi}} < 1, \\ 1, & \bar{\bar{\xi}} \geqslant 1. \end{cases} \tag{2.4}$$

The height, width, location and shape of the roughness element all influence the amplitude A of the triggered instability. Normalizing A by the roughness amplitude

defines the receptivity coefficient C_r for wall roughness,

$$C_r(\lambda_z; \xi_r, \varepsilon_r) \equiv \frac{A_{rs}(\lambda_z; \xi_r, \varepsilon_r)}{\varepsilon_r}, \qquad (2.5)$$

where A_{rs} denotes the amplitude of the excited Görtler mode at the receptivity site (the roughness station ξ_r) and is referred to as receptivity amplitude. For linear receptivity mechanisms, C_r is constant upon varying the bump height ε_r. In that case, the disturbance velocity enforced by the roughness is proportional to the local roughness height. This motivates a widely used roughness model: instead of meshing the bump $h(\xi, z)$, the effect of the roughness is imposed as an inhomogeneous boundary condition for the perturbation velocity $\boldsymbol{u}$ ('domain perturbation method'; cf. Cabal, Szumbarski & Floryan 2001), using a first-order Taylor series expansion around the smooth wall (subscript 0),

$$\boldsymbol{u}_0 = -h(\xi, z) \left(\frac{\partial \boldsymbol{U}_b}{\partial \eta} \right)_0. \qquad (2.6)$$

The roughness model translates via the wall gradient of the base flow the zero-slip condition at the rough wall to a local slip at the smooth wall (figure 2b). The present model is by construction valid only for linear receptivity, i.e. for small-amplitude roughness. Schrader, Brandt & Henningson (2009) found in swept-plate flow that the model fails for $\varepsilon_r \gtrsim 5\%$ of the local boundary-layer displacement thickness. Here, we shall compare for Görtler flow the linear roughness model with the meshed roughness.

2.3.2. *Vortical modes*

The free-stream vortical disturbances are modelled by Orr–Sommerfeld continuous-spectrum modes for the Blasius inflow (Grosch & Salwen 1978). In the free stream, the Orr–Sommerfeld and Squire equations simplify to constant-coefficient homogeneous ordinary differential equations in the wall-normal coordinate η and are decoupled from each other. The Orr–Sommerfeld equation can therefore be solved alone to obtain the wall-normal velocity, while the wall-normal vorticity, solution to the Squire equation, is set to zero. In Fourier space the Orr–Sommerfeld equation reads

$$\left. \begin{array}{l} \left(\dfrac{\mathrm{d}^2}{\mathrm{d}\eta^2} - \alpha^2 - \beta^2 \right) \left(\dfrac{\mathrm{d}^2}{\mathrm{d}\eta^2} + \gamma^2 \right) \hat{v} = 0, \\[2mm] \hat{v} = \dfrac{\mathrm{d}\hat{v}}{\mathrm{d}\eta} = 0 \quad \text{for } \eta = 0, \\[2mm] \hat{v} \text{ bounded} \quad \text{for } \eta \to \infty, \end{array} \right\} \qquad (2.7)$$

where $\hat{v}$ is the shape function of the wall-normal disturbance velocity and α and β are the streamwise and spanwise wavenumbers, respectively. The quantity $\gamma^2 \equiv -\mathrm{i}Re_{\delta^*}(\alpha U_\infty - \omega) - \alpha^2 - \beta^2$ plays the role of a wall-normal wavenumber, where ω is the angular frequency of the mode. The expression for γ also constitutes the dispersion relation of the free-stream waves and is used to calculate the complex streamwise wavenumber α for given values of Re_{δ^*}, ω, β and γ. Once the wavevector is known, (2.7) is solved numerically employing a boundedness condition for $\hat{v}$ (Jacobs & Durbin 1998). The streamwise and spanwise components $\hat{u}$ and $\hat{w}$ of the free-stream modes are calculated using the continuity equation and the definition of wall-normal vorticity (zero here). This yields $\hat{u} = \mathrm{i}\alpha/(\alpha^2 + \beta^2) \, \mathrm{d}\hat{v}/\mathrm{d}\eta$ and $\hat{w} = \mathrm{i}\beta/(\alpha^2 + \beta^2) \, \mathrm{d}\hat{v}/\mathrm{d}\eta$. Figure 3(a) displays the wall-normal profile $\hat{\boldsymbol{u}} = (\hat{u}, \hat{v}, \hat{w})$ of an Orr–Sommerfeld free-stream mode. The disturbance oscillates in the free stream and is damped towards
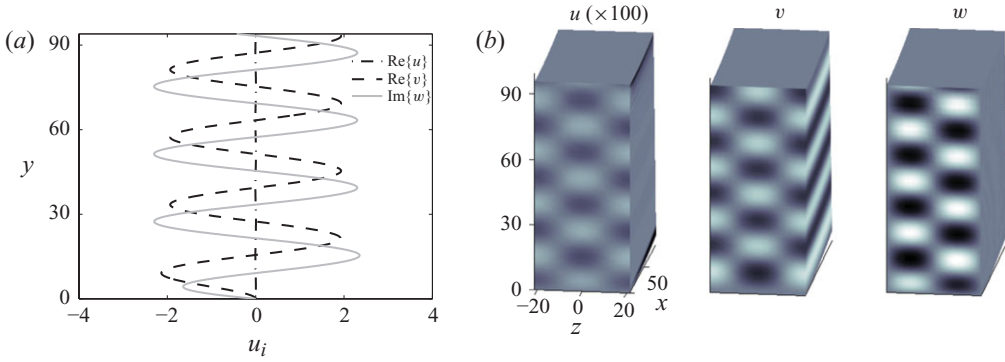
FIGURE 3. (Colour online) (*a*) Complex wall-normal profile of the Orr–Sommerfeld continuous-spectrum mode with $F = 0$, $\beta = 0.147$ ($\Lambda = 1790$) and $\gamma = 0.262$; only the non-zero real (Re) and imaginary (Im) parts of the streamwise, wall-normal and spanwise disturbances u, v and w (denoted by placeholder u_i) are shown. (*b*) Inflow disturbance constructed from the free-stream vortical mode in (*a*); white/black: $u_i = \pm 2.5$; u multiplied by 100.

the wall. The detailed structure of the continuous-spectrum modes was explained by Zaki & Saha (2009). Here, the real part (Re) of these modes is specified at the inflow plane ξ_{in},

$$\boldsymbol{u}_{in} = \text{Re}\{\hat{\boldsymbol{u}}(\gamma \eta)\, \mathrm{e}^{\mathrm{i}(\alpha \xi_{in} + \beta z - \omega t)}\}, \qquad (2.8)$$

as shown in figure 3(*b*). Normalizing ω gives the frequency parameter

$$F = \frac{\omega}{U_\infty^2 / \nu} \times 10^6. \qquad (2.9)$$

The frequency, amplitude and wavevector of the free-stream disturbance all influence the amplitude A of the triggered instability, which hence is conveniently normalized as

$$C_v(F, \beta; \gamma, \varepsilon_v) \equiv \frac{A_{rs}(F, \beta; \gamma, \varepsilon_v)}{\varepsilon_v}. \qquad (2.10)$$

This defines the receptivity coefficient C_v for free-stream vortical modes. The receptivity amplitude A_{rs} of the excited Görtler mode is evaluated at the inflow plane, and ε_v is the inflow amplitude of the modes,

$$\varepsilon_v = \sqrt{\frac{1}{3}\overline{\boldsymbol{u}^2}_{in}}. \qquad (2.11)$$

The bar denotes averaging in the spanwise direction and over one wall-normal wavelength in the free stream. For linear receptivity mechanisms, C_v is constant upon varying the disturbance amplitude ε_v.

2.4. Results

2.4.1. Base flow

Figures 4(*a*) and 4(*b*) depict the pressure distribution in the flow field over the plate with radius $R^* = 1\,\text{m}$. The radial gradient of the centrifugal force enforces a wall-normal pressure gradient in the free stream, which relaxes towards $\partial p / \partial \eta \approx 0$ inside the boundary layer (inset of figure 4*a*). In the streamwise direction, the pressure decreases slowly at the wall while being nearly constant in the free stream (figure 4*b*). The Görtler boundary layer grows in thickness at nearly the same rate as the Blasius boundary layer (figure 4*c*). Floryan & Saric (1982) demonstrate that the basic state
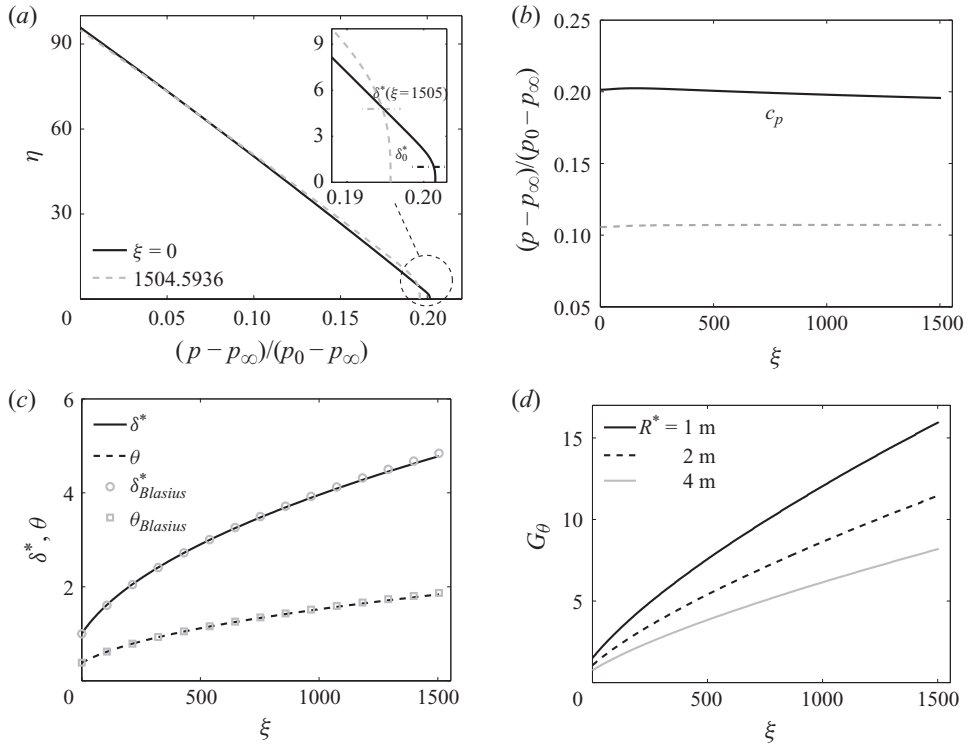
FIGURE 4. (*a*) Wall-normal distribution of the normalized pressure at the computational inflow (solid) and outflow (dashed). (*b*) Normalized pressure in the free stream ($\eta = 47.9$, dashed line) and pressure coefficient. (*c*) Displacement and momentum-loss thickness. (*d*) Local Görtler number for $R^* = 1$, 2 and 4 m.

is not affected by surface curvature if $Re \to \infty$. Thus, in the large-Re limit, a Görtler boundary layer can be approximated by Blasius profiles (see also Boiko *et al.* 2010, figure 4*a*), which justifies our choice of inflow and free-stream boundary conditions. Figure 4(*d*) shows the streamwise evolution of the local Görtler number on the plates with radius $R^* = 1$, 2 and 4 m.

2.4.2. *Görtler instability*

Figure 5 displays the Görtler boundary-layer response ($R^* = 1$ m) to upstream localized surface roughness. Longitudinal structures of amplifying positive and negative streamwise disturbance velocities develop, the spanwise wavelength of which is constant in the streamwise direction (figure 5*a*). The cross-stream velocity components establish a counter-rotating motion of longitudinal vortex pairs, accompanied by positive and negative streamwise-velocity disturbances in the downwash and upwash regions between two adjacent vortices (figure 5*b*). Centrifugal instability modes are thus made up of pairs of counter-rotating longitudinal vortices (Görtler rolls) and a pattern of low- and high-speed streamwise disturbances. Farther downstream, the vortex axes are lifted away from the wall, and the low-speed region exhibits a highly distorted mushroom-like shape due to strong nonlinear interactions (figure 5*c*).

Figure 6(*a*) depicts the linear spatial evolution of the steady Görtler mode with wavelength $\Lambda = 250$. This mode amplifies the most within our computational domain
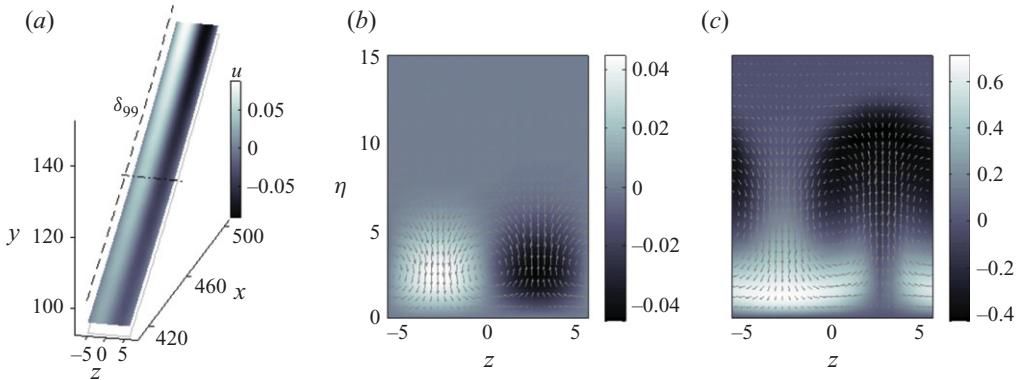
FIGURE 5. (Colour online) Spatial evolution of a steady Görtler mode with spanwise wavenumber $\beta = 0.546$ ($\Lambda = 250$) on a plate with radius $R^* = 1\,\text{m}$ due to upstream surface roughness. (a) Structure of the mode in the linear range. The dash-dotted line marks the station of the cross-section in (b). Streamwise (grey scale), wall-normal and spanwise disturbance velocities (vectors) at (b) $G_\theta = 7.4$ and (c) $G_\theta = 11$.

and is referred to as 'the most unstable mode' in the following (although other modes may become more energetic farther downstream). The modal evolution has been obtained from linearized Navier–Stokes computations with an inflow condition containing the Görtler mode. The shape of this inflow mode was extracted from a preliminary simulation of a fully developed Görtler mode and re-scaled in size and amplitude to match the inflow conditions of the main simulation. This approach was verified by an additional simulation with a smaller inlet Reynolds number ($Re_{\delta_0^*} = 74.8$ instead of 198.36) in order to clarify the sensitivity of the upstream disturbance evolution to the inflow conditions. The evolution curves from the auxiliary and the main simulation are hardly distinguishable in the region of overlap (figure 6a, inset). Such evolution curves will later be used to extract the receptivity coefficients. Figure 6(b) shows the streamwise development of steady Görtler modes on three plates with radius $R^* = 1$, 2 and 4 m. When plotted versus G_θ, the evolution curves collapse, which highlights the role of the Görtler number as the relevant instability parameter. Figure 6(c) depicts the local growth rates of Görtler modes with various spanwise wavelengths, calculated by linearized simulations. Except for the largest-wavelength mode ($\Lambda = 1790$) all modes are unstable already at $G_\theta = 3$. Far downstream, the fastest-growing Görtler mode is that with $\Lambda = 250$ (see Mitsudharmadi, Winoto & Shah 2004). The modes in the range $160 \leqslant \Lambda \leqslant 273$ feature similar growth rates, i.e. there is no pronounced wavelength selection in Görtler boundary layers in this Λ-regime. For this reason, variations of the upstream conditions in wind-tunnel experiments led to Görtler modes with different spanwise scales (Swearingen & Blackwelder 1983). Figure 6(d) shows the local growth rates of Görtler modes with various frequencies, indicating that Görtler boundary layers are also unstable to travelling Görtler vortices. In fact, the low-frequency Görtler mode ($F = 16$) amplifies at nearly the same rate as the most unstable steady Görtler roll.

2.4.3. *Receptivity to surface roughness*

Figure 7(a) shows the boundary-layer response to a meshed roughness element placed at $\xi_r = 30.1$. The spanwise wavenumber of the roughness is $\beta = 0.546$ ($\Lambda = 250$) and the bump height is $\varepsilon_r = 0.01\delta_r^*$, where δ_r^* is the displacement thickness at ξ_r. The roughness-induced perturbation is concentrated in the streamwise component
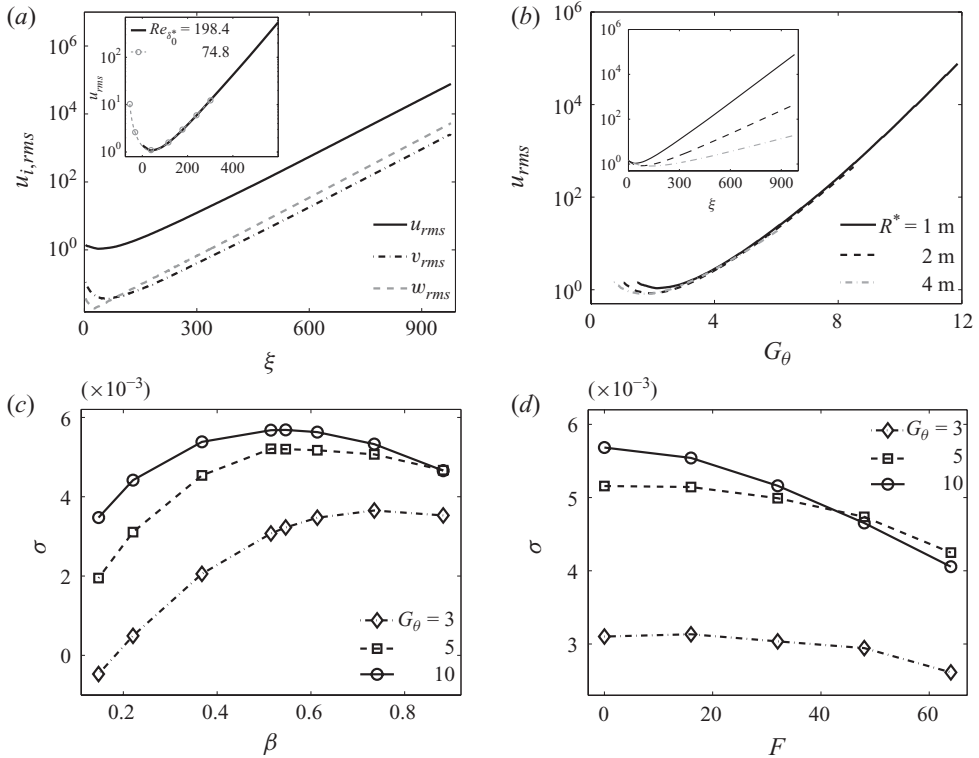
FIGURE 6. Görtler instability. (*a*) Streamwise evolution of u_{rms}, v_{rms} and w_{rms} (wall-normal maximum of spanwise root-mean-square (r.m.s.) of streamwise, wall-normal and spanwise velocity) of the most unstable steady mode ($\beta = 0.546$; $\Lambda = 250$) on a plate with $R^* = 1$ m. (*b*) Evolution of the most unstable steady mode on plates with $R^* = 1$, 2 and 4 m. (*c*) Local growth rates of steady Görtler modes versus spanwise wavenumber (symbols from left to right: $\Lambda = 1790$, 975, 453, 273, 250, 210, 160, 122) at three streamwise locations. (*d*) Local growth rates of Görtler modes ($\Lambda = 250$) versus frequency.

and – after some initial decay – soon evolves into a mode with exponential amplification. Farther downstream, nonlinear processes cause the saturation of this mode and the emergence of higher harmonics (figure 7*b*). Moreover, a spanwise-independent mean-flow distortion is seen, obtained after a subtraction of the laminar reference state. This suggests that the original laminar flow is modified due to the presence of the roughness element.

Variation of roughness width. Figure 8(*a*) shows the influence of the spanwise roughness scale on the receptivity coefficient C_r (cf. (2.5)). The receptivity amplitude A_{rs} of the Görtler mode, defined here as u_{rms}, is obtained by matching the evolution of the mode (e.g. figure 6*a*) with the response to the roughness element (e.g. figure 7*a*). The contribution of the Görtler mode to the total disturbance can then be traced back to the receptivity site, i.e. the roughness station. We find maximum receptivity for a spanwise wavenumber of $\beta = 0.368$ ($\Lambda = 453$), which differs from the most unstable wavenumber ($\beta = 0.546$; $\Lambda = 250$). Farther downstream ($G_\theta = 5$, figure 8*b*), modes with smaller scales become dominant owing to their larger growth rates. The largest amplitude is attained by the Görtler mode with $\beta = 0.614$ ($\Lambda = 210$), while the most unstable mode is still somewhat weaker.
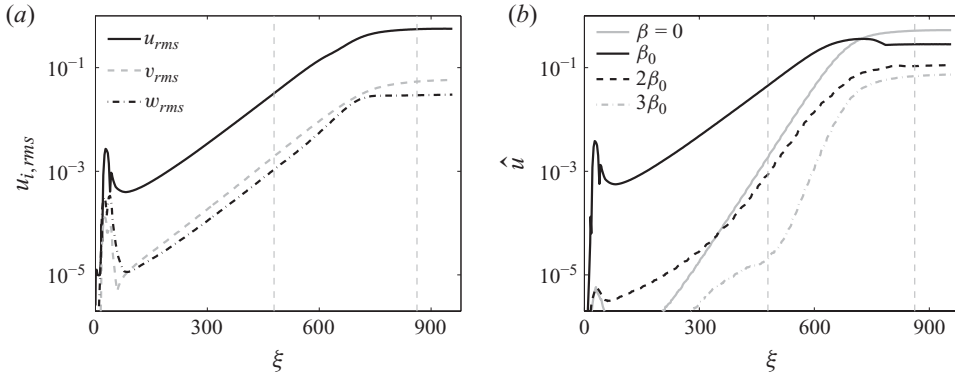
FIGURE 7. Boundary-layer response ($R^* = 1\,\text{m}$) to meshed, localized roughness with spanwise wavenumber $\beta = 0.546$ ($\Lambda = 250$), height $\varepsilon_r = 0.01\delta_r^\star$, location $\xi_r = 30.1$ and shape defined by $\Delta\xi_r = 30.1$ and $\Delta\xi_{rise} = \Delta\xi_{fall} = 15.0$ (see figure 2a). (a) Wall-normal maximum of u_{rms}, v_{rms} and w_{rms}. (b) Decomposition of the boundary-layer disturbance into contributions with $\beta = 0$, $\beta_0 = 0.546$, $2\beta_0$ and $3\beta_0$. The stations marked by dashed grey lines correspond to those of figures 5(b) and 5(c).
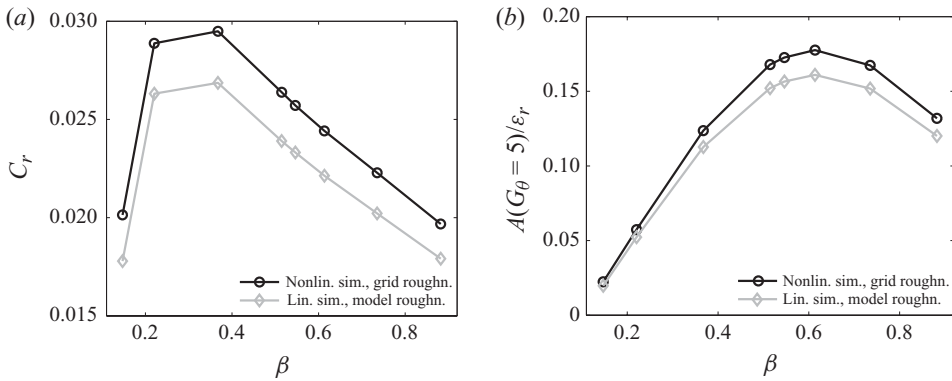

FIGURE 8. Flow response ($R^* = 1\,\text{m}$) to roughness bumps ($\varepsilon_r = 0.01\delta_r^\star$, $\xi_r = 30.1$, shape: see caption of figure 7) with various spanwise wavenumbers. Comparison between results from nonlinear (nonlin.) computations with meshed roughness (roughn.) and those from linear simulations (sim.) with the model roughness. (a) Receptivity coefficient versus spanwise wavenumber. Symbols (from left to right) mark $\Lambda = 1790$, 975, 453, 273, 250, 210, 160 and 122. (b) Downstream amplitudes (normalized by ε_r) of the Görtler modes at the local Görtler number $G_\theta = 5$.

Variation of roughness height. Figure 9(a) shows the boundary-layer response to roughness elements with various heights in the range $0.01\delta_r^\star \leqslant \varepsilon_r \leqslant 0.4\delta_r^\star$. The spanwise scale and streamwise location of the bumps are $\Lambda = 250$ and $\xi_r = 30.1$, respectively. In figure 9(b), the receptivity coefficient for meshed roughness is seen to be nearly constant over the range of roughness heights considered. This indicates that the receptivity of the Görtler boundary layer is linear in the roughness amplitude even for high bumps ($\varepsilon_r = 40\,\%\ \delta_r^\star$). In contrast, Schrader *et al.* (2009) found in swept-plate flow that roughness receptivity becomes nonlinear already for bumps with much lower amplitudes ($\approx 5\,\%$ of $\delta_r^\star$).

Linear roughness model. So far, we have only considered the flow response to meshed wall-roughness elements. Figures 8 and 9 also show results obtained when using the linear roughness model (see §2.3.1). This model offers numerical simplicity
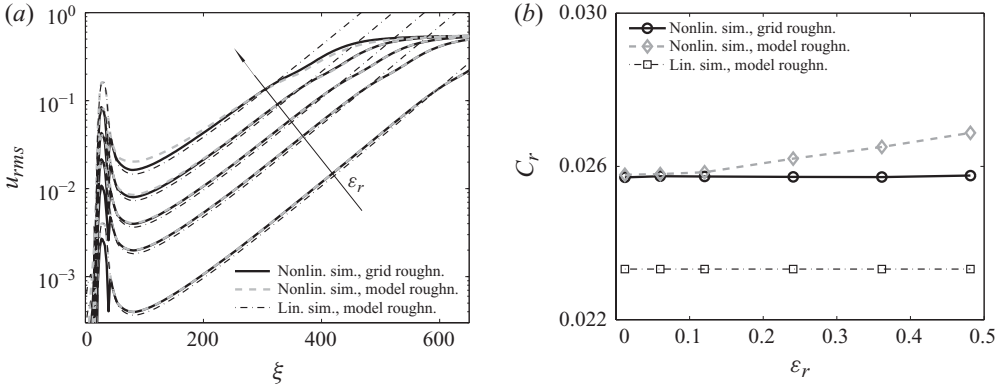
FIGURE 9. (a) Boundary-layer response ($R^* = 1$ m) to roughness ($\Lambda = 250$, $\xi_r = 0.01\pi$, shape: see caption of figure 7) of various heights: $\varepsilon_r = 1\%$, 5%, 10%, 20% and 40% of δ_r^* (displacement thickness at ξ_r). Comparison of nonlinear and linear simulations with meshed and modelled roughness. (b) Receptivity coefficients versus roughness height. Note that ε_r is scaled by δ_0^* rather than $\delta_r^\star$.

and was therefore used in numerous receptivity studies (e.g. Ng & Crouch 1999; Schrader *et al.* 2009). However, figure 8(a) shows that the receptivity coefficients predicted by linearized Navier–Stokes computations with the linear roughness model are about 10 % lower than those from nonlinear Navier–Stokes simulations with meshed roughness. This leads to underprediction of the downstream amplitude of the Görtler rolls in the linear framework (figure 8b). Figure 9(a) shows that the failure of the linear roughness model is mainly due to a discrepancy in the transient region near the bump. In particular, the transient decay at the modelled roughness is larger than that at the meshed bump. It is remarkable that the difference between the receptivity coefficients from the nonlinear and the linear calculations does not increase for higher bumps (figure 9b). The prediction of roughness receptivity can be improved if the roughness model is combined with nonlinear instead of linearized Navier–Stokes computations. For bump heights up to 20 % of $\delta_r^\star$, this leads to a significantly better prediction of the downstream amplitude of the Görtler mode (figure 9a) and the receptivity coefficients (figure 9b). We summarize that studies of Görtler boundary-layer receptivity to wall roughness should use meshed roughness rather than bump models based on velocity boundary conditions. The limitation of such models was also pointed out by Cabal *et al.* (2001) for a study of channel flow with corrugated walls.

Variation of roughness location. Figure 10(a) shows the evolution of the boundary-layer disturbance (radius $R^* = 1$ m) for roughness elements at four different streamwise stations. The roughness amplitude is kept constant with respect to the local displacement thickness ($\varepsilon_r = 1\% \delta_r^\star$). We note that the Görtler mode does not emerge faster when triggered farther downstream, although the flow conditions become more unstable. This is reflected by a downstream decreasing receptivity coefficient. Moreover, roughness receptivity decreases when the wall radius is increased (figure 10b). We demonstrate in figure 10(c) that radius-independent results can be obtained when scaling the receptivity coefficient by the square root of the local Görtler number and plotting it versus the local Reynolds number. This finding suggests that receptivity to localized wall roughness scales as $C_r \propto \sqrt{G_\theta}$.
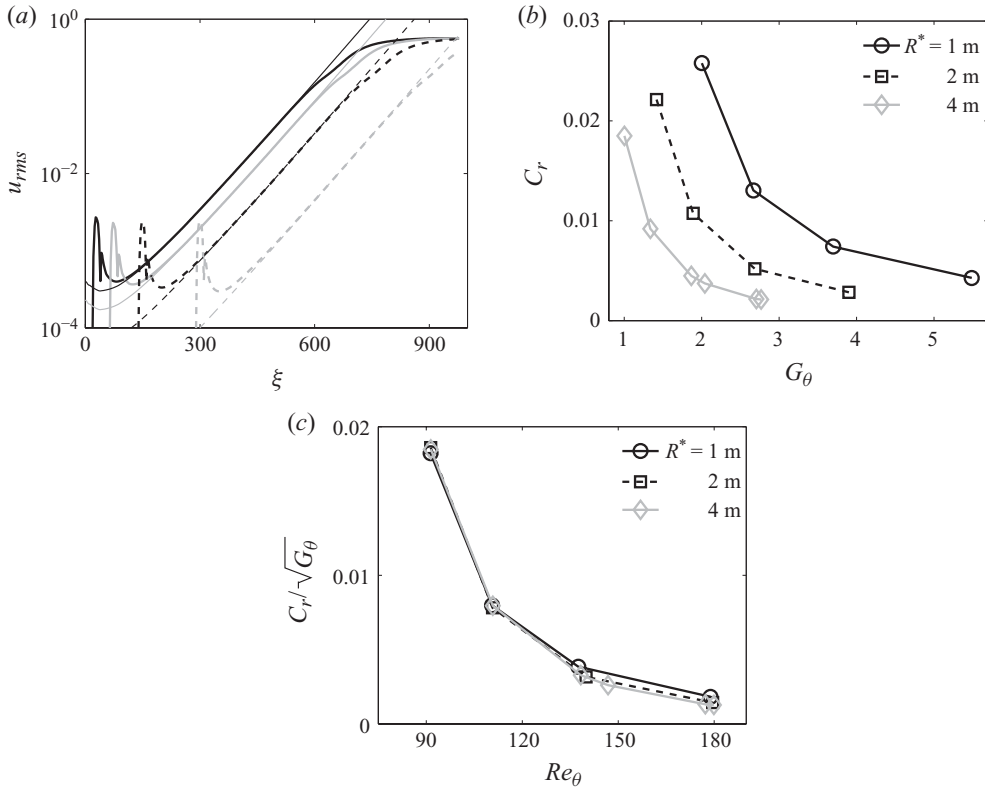
FIGURE 10. (*a*) Streamwise evolution of u_{rms} in Görtler boundary layer ($R^* = 1$ m) with meshed surface roughness (thick lines; $\varepsilon_r = 0.01\delta_r^*$, $\beta = 0.546$ ($\Lambda = 250$), shape: see figure 7, caption) and evolution of the corresponding Görtler mode (thin lines). (*b*) Receptivity coefficients of Görtler boundary layers with radius $R^* = 1$, 2 and 4 m. Note that, while β is constant Λ changes with R^* and is 250, 177 and 125, respectively. (*c*) Receptivity coefficients of (*b*), scaled by square root of the local Görtler number, versus Reynolds number.

Variation of roughness shape. Three different roughness elements are considered, differing in their streamwise length and the steepness of the flanks of the step function (table 2). The streamwise location and the height of the roughness are kept constant. Figure 11 shows that the longest (least localized) bump excites Görtler rolls with higher amplitude than the two shorter bumps. The Görtler boundary layer hence becomes more receptive when the roughness is less localized in the streamwise direction (cf. C_r values in table 2). Similarly, Denier *et al.* (1991) found that streamwise-distributed wall roughness is more important than isolated roughness elements. It is known that roughness shape-independent results can be obtained, if the receptivity coefficients are normalized by the Fourier amplitude of the streamwise roughness shape pertaining to the unstable mode. An example is given in Schrader *et al.* (2009) for swept-plate boundary layers, where the receptivity coefficient is defined as

$$C_{r,alt} = \frac{A_{rs}}{\varepsilon_r H(\alpha_{mode})}. \tag{2.12}$$

The quantity α_{mode} is the streamwise wavenumber of the triggered boundary-layer mode, and $H(\alpha_{mode})$ is the Fourier coefficient of the normalized streamwise roughness contour pertaining to α_{mode}. We tested the validity of (2.12) in Görtler flow, where
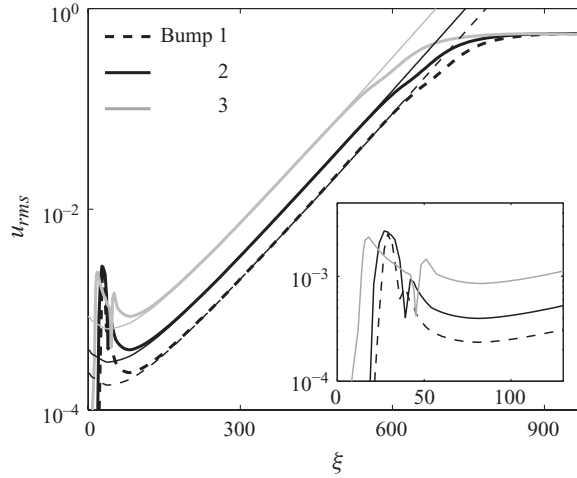
FIGURE 11. Receptivity to three bumps ($\varepsilon_r = 0.01\delta_r^\star$, $\Lambda = 250$) with different streamwise shapes. Thick lines show flow response ($R^* = 1\,\text{m}$) to meshed, localized wall roughness with the three shapes compiled in table 2. Thin lines show evolution of the Görtler mode with $\Lambda = 250$.

Bump	1	2	3
ξ_r	30.1	30.1	30.1
$\Delta\xi_r$	18.1	30.1	42.1
$\Delta\xi_{rise}$	9.05	15.05	10.05
$\Delta\xi_{fall}$	9.05	15.05	10.05
$C_r(\times 10^{-2})$	1.52	2.57	5.51

TABLE 2. Receptivity coefficients for three bumps ($\varepsilon_r = 0.01\delta_r^\star$, $\Lambda = 250$) with different streamwise shapes.

the steady Görtler vortices have $\alpha_{mode} = 0$. It turned out that no shape-independent value of $C_{r,alt}$ could be obtained, i.e. the normalization by $H(0)$ is inappropriate for the present configuration. The inset in figure 11 gives a possible explanation, showing that the transient disturbances near the roughness are fairly different for the three bumps considered. These transients are built up by a wide range of modes with different streamwise scales excited by the roughness elements and play a key role in the receptivity of Görtler flow to wall roughness. In contrast, Schrader *et al.* (2009) showed that 'wavenumber resonance' at α_{mode} between the roughness element and the boundary-layer instability is key of the receptivity mechanism in swept-plate boundary layers.

2.5. *Receptivity to vortical modes*

Free-stream vortical modes prescribed at the inflow plane are also able to excite amplifying boundary-layer disturbances (figure 12*a*). Rapid non-modal growth of the streamwise disturbance is seen near the inflow plane, whereas the wall-normal and spanwise disturbance components initially attain their wall-normal maxima outside the boundary layer. This type of disturbance, referred to as streak or Klebanoff mode, also exists in flat-plate boundary layers exposed to free-stream perturbations. Farther downstream, the three components of the boundary-layer disturbance amplify
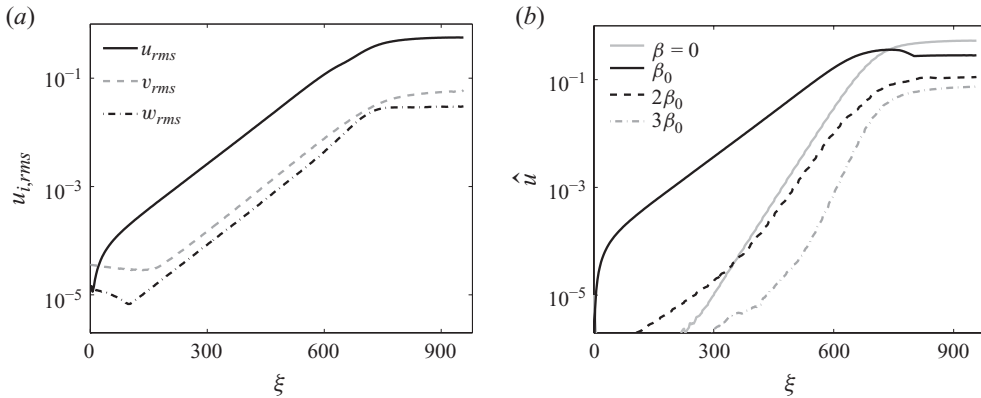
(a)

(b)

FIGURE 12. Boundary-layer response ($R^* = 1$ m) to a single free-stream vortical mode ($\beta = 0.546$, $\gamma = 0.262$, $F = 0$, $\varepsilon_v = 1.67 \times 10^{-5}$). (a) Wall-normal maximum of u_{rms}, v_{rms} and w_{rms} (temporal-spanwise r.m.s.) versus streamwise coordinate. (b) Decomposition of the boundary-layer disturbance into contributions with $\beta = 0$, $\beta_0 = 0.546$, $2\beta_0$ and $3\beta_0$.

exponentially, indicating the emergence of a modal instability. This mode saturates as shown in figure 12(b), where a substantial mean-flow modification ($\beta = 0$) is also seen.

Comparing figures 12 and 7 yields that the Görtler rolls excited by the steady free-stream vortical mode attain similar amplitudes as those due to surface roughness with height $\varepsilon_r = 0.01\delta_r^\star$, despite the low intensity of the free-stream disturbance ($\varepsilon_v = 1.67 \times 10^{-5}$). This suggests that Görtler boundary layers are highly receptive to steady free-stream vorticity. The associated receptivity mechanism is linear in the amplitude of the free-stream forcing (verified by considering different values of ε_v). It is evident in figure 12 that the initial transient growth of boundary-layer streaks plays a crucial role for the initiation of the centrifugal instability. The Görtler mode emerges from the upstream streaks and becomes dominant farther downstream. The potential of free-stream disturbances as triggers of centrifugal instability was also pointed out by Cossu *et al.* (2000), whose optimal inflow perturbations reached outside the edge of the boundary layer, hence coupling efficiently to free-stream disturbances.

Variation of wave vector. Receptivity coefficients for free-stream vortices with various spanwise wavenumbers β are plotted in figure 13(a). The Görtler boundary layer is most receptive to vortical modes with small values of β. However, because Görtler rolls with larger β amplify at higher rates (cf. figure 6c), these become dominant over the small-β modes farther downstream (figure 13b). The dependence of the receptivity coefficient on the wall-normal wavenumber γ is opposite to that on β, where maximum receptivity is obtained for large-γ free-stream modes (figure 13c). These modes penetrate more deeply into the boundary layer than the small-γ vortical modes (figure 13d; see also Zaki & Durbin 2005, figure 5); moreover, the coupling between the Orr–Sommerfeld mode and the associated set of Squire modes is stronger. This is indicated by $|v|U_b'$ (figure 13e), where U_b' is the wall-normal derivative of the Blasius streamwise-velocity profile. The forcing of Squire modes by the Orr–Sommerfeld mode is crucial for the amplification of boundary-layer streaks (Zaki & Durbin 2005), and thus of the Görtler modes. The large-γ free-stream mode also introduces larger streamwise vorticity into the boundary layer than the small-γ mode (figure 13f). Streamwise vorticity is key to the lift-up mechanism of streak generation.

It is interesting to compare the receptivity to free-stream vortical modes (figure 13a) with that to surface roughness (figure 8a). For Görtler rolls with $\beta = 0.546$ ($\Lambda = 250$),
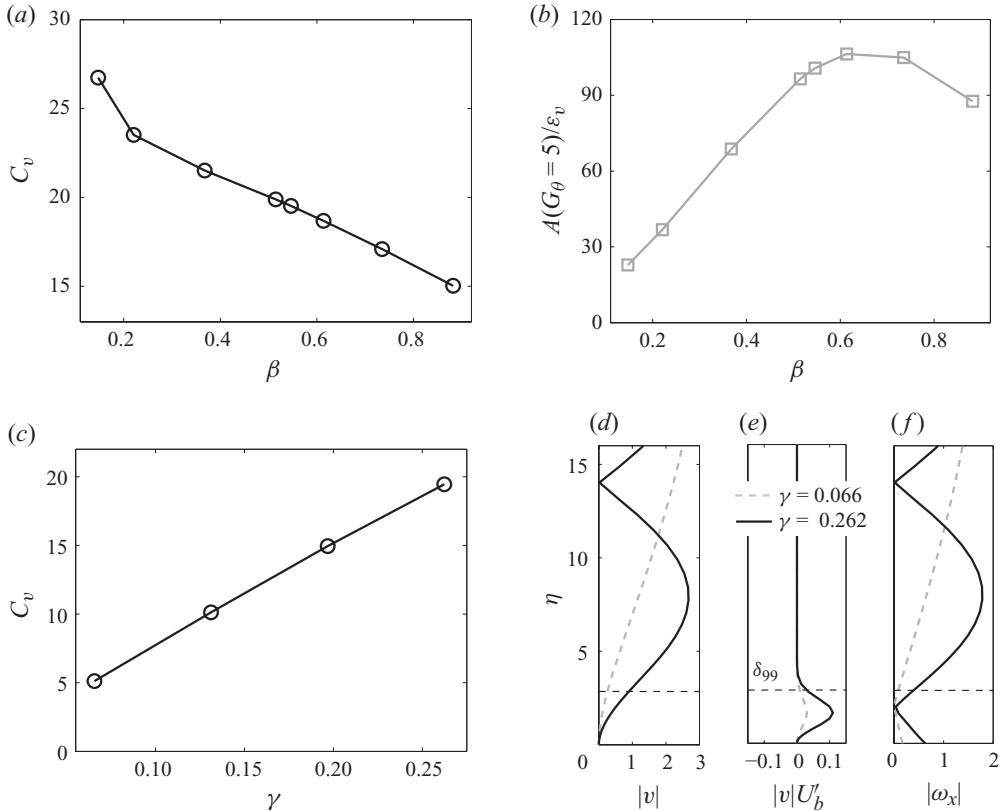
FIGURE 13. Response of the Görtler flow ($R^* = 1$ m) to steady free-stream vortical modes with different wavevectors. (a) Receptivity coefficient versus spanwise wavenumber of the free-stream modes ($\gamma = 0.262$). Symbols (from left to right) show $\Lambda = 1790$, 975, 453, 273, 250, 210, 160 and 122. (b) Local amplitude of the Görtler modes at $G_\theta = 5$, normalized by ε_v. (c) Receptivity coefficient versus wall-normal wavenumber of the free-stream modes ($\beta = 0.546$). Magnitude of (d) wall-normal velocity and (f) streamwise vorticity of steady free-stream modes ($\beta = 0.546$) with two different values of γ. The quantity $|v/U_b'|$ shown in (e) is a measure for the coupling between the Orr–Sommerfeld mode and the associated set of Squire modes.

for instance, the height of bump 1 (2, 3) must be 2.15 (1.27, 0.59) $\times 10^{-2} \delta_r^*$ in order to generate the same amplitude Görtler instability as the steady free-stream mode with amplitude $1.67 \times 10^{-5} U_\infty$. For a meaningful comparison with the free-stream modal amplitude, the roughness height must be translated into a disturbance velocity. We use the linear roughness model (2.6) for this purpose and write the roughness-induced velocity disturbance amplitude as $\tilde{\varepsilon}_r = \sqrt{\overline{\boldsymbol{u}_0^2(\xi_r)}/3}$ in analogy with (2.11), where $\boldsymbol{u}_0(\xi_r)$ is obtained from (2.6), ξ_r is the roughness station and the bar denotes spanwise averaging. This yields $\tilde{\varepsilon}_r = 4.16$ (2.46, 1.14) $\times 10^{-3} U_\infty$ for bump 1 (2, 3), i.e. two orders-of-magnitude larger values than the free-stream modal amplitude. Steady free-stream vortical disturbances hence appear to be more likely and efficient triggers of Görtler rolls than localized wall roughness; in particular, they give rise to significantly stronger transient growth of steady streaks evolving into the Görtler rolls.

Variation of frequency. Görtler boundary layers are also receptive to unsteady free-stream vorticity (figure 14a). In that case, the upstream non-modal disturbances
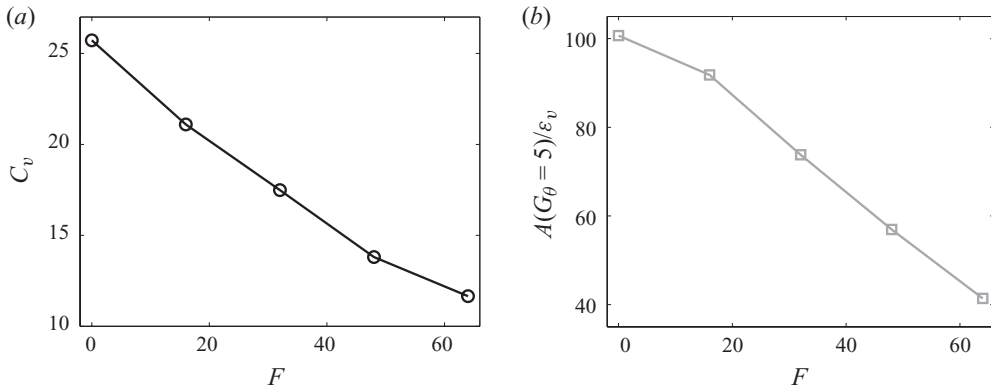
FIGURE 14. (*a*) Receptivity coefficients in Görtler flow ($R^* = 1\,\mathrm{m}$) for free-stream vortical modes ($\beta = 0.546$, $\gamma = 0.262$) with various frequencies. (*b*) Normalized downstream amplitude ($G_\theta = 5$) of travelling Görtler vortices versus frequency of the free-stream modes.

develop into travelling Görtler modes. The receptivity coefficient is, however, smaller than that for the steady Görtler mode and drops with increasing frequency, which explains the downstream dominance of the steady Görtler rolls over the travelling Görtler vortices (figure 14*b*). Because the travelling Görtler mode of lowest frequency ($F = 16$) is only about 10 % weaker than the steady mode, it may become important under certain disturbance conditions (see Schultz & Volino 2003 for instance). Unsteady Görtler vortices have been largely overlooked in the literature, which is almost entirely devoted to the steady rolls. An exception is the recent experimental work by Boiko *et al.* (2010), who considered both quasi-steady and unsteady Görtler instabilities.

Nonlinear receptivity. In flat-plate boundary layers, there exists a nonlinear receptivity mechanism to high-frequency free-stream disturbances (Berlin & Henningson 1999). This mechanism consists of two steps, first the nonlinear generation of streamwise-vorticity modes with zero frequency and doubled spanwise wavenumber and subsequently the linear formation of streamwise-velocity streaks (Brandt, Henningson & Ponziani 2002). Here, we investigate by nonlinear DNS whether nonlinear receptivity is also available in Görtler boundary layers. The inflow disturbance consists of a pair of continuous-spectrum Orr–Sommerfeld modes with frequency F and spanwise wavenumbers $\pm\beta$, thus representing two free-stream waves with opposite angles of incidence ('oblique modes'). The wavenumber β chosen is approximately half the value of the most unstable steady Görtler mode. Two different forcing frequencies and amplitudes are considered. At the lower frequency ($F = 64$), the boundary-layer disturbance is dominated by the fundamental travelling Görtler vortex due to linear receptivity (figure 15*a*). A steady Görtler mode with twice the fundamental spanwise wavenumber and a mean-flow modification ($\beta = 0$) are also seen, but these nonlinear contributions are weaker than the fundamental mode. The opposite holds if the forcing frequency is doubled ($F = 128$, figure 15*b*). The steady Görtler mode due to nonlinear effects is now dominant, whereas no unsteady mode emerges. When multiplying the amplitude of the inflow perturbation by 10 (figure 15*c*), the steady Görtler vortex attains a 100 times larger amplitude, indicating a quadratic receptivity mechanism. It is concluded that two competing unsteady receptivity mechanisms can be at play simultaneously in Görtler boundary layers (depending on F): a linear mechanism, exciting a travelling Görtler mode, and
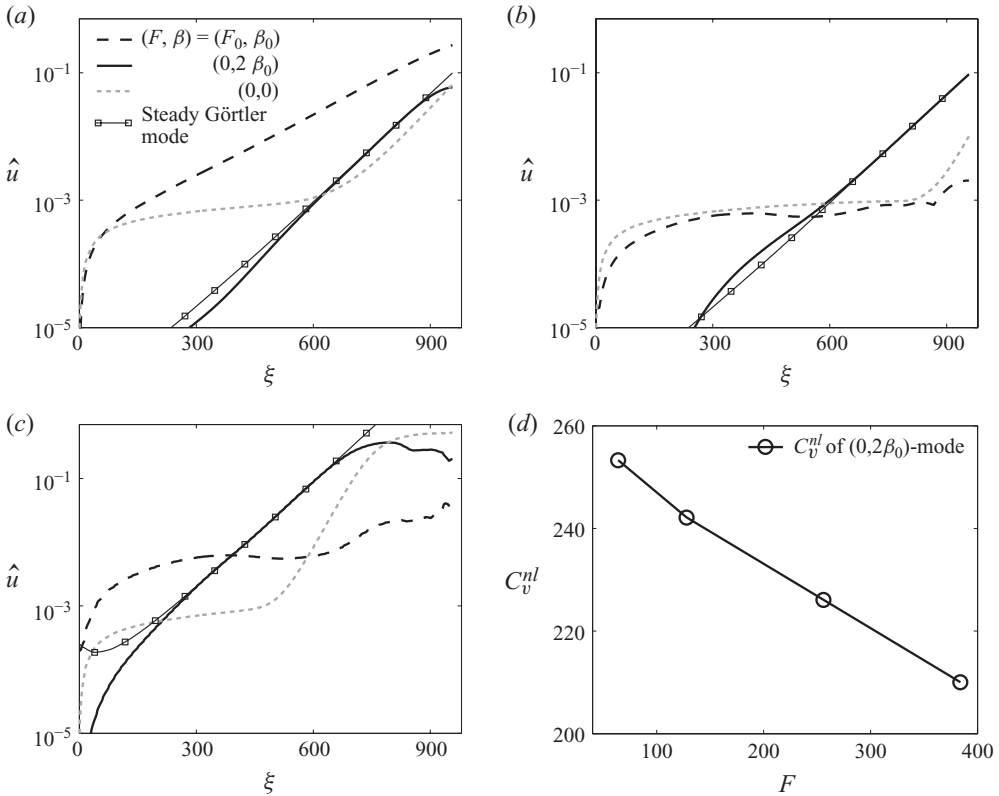
FIGURE 15. Response of Görtler flow ($R^* = 1\,\mathrm{m}$) to two oblique unsteady free-stream vortical modes ($\beta_0 = 0.257$ ($\Lambda = 773$), $\gamma = 0.262$). Decomposition of the boundary-layer disturbance into contributions with different frequencies and spanwise wavenumbers. The evolution of the steady Görtler mode with $\beta = 2\beta_0 = 0.515$ ($\Lambda = 273$, dashed, squares) is shown for comparison. Oblique modes with (a) $F = 64$, $\varepsilon_v = 8.6 \times 10^{-5}$; (b) $F = 128$, $\varepsilon_v = 8.6 \times 10^{-5}$; (c) $F = 128$, $\varepsilon_v = 8.6 \times 10^{-4}$. (d) Nonlinear receptivity coefficient for the steady Görtler mode with $\beta = 2\beta_0$ ($\Lambda = 273$) versus frequency of the forcing oblique modes.

a nonlinear mechanism, triggering steady Görtler rolls. A threshold of the forcing amplitude ε_v can be determined, beyond which the steady Görtler mode attains a larger amplitude at a fixed streamwise position than the fundamental travelling mode. For $F = 64$ and $G_\theta = 9$ ($\xi = 641$), this threshold is $\varepsilon_{v,thres} = 2 \times 10^{-3}$.

Figure 15(d) depicts the receptivity coefficient for the steady Görtler mode $(0, 2\beta_0)$. Since the receptivity of this mode is quadratic in ε_v, the correct normalization is

$$C_v^{nl}(F, \beta; \gamma, \varepsilon_v) = \frac{A_{rs}(F, \beta; \gamma, \varepsilon_v)}{\varepsilon_v^2}, \tag{2.13}$$

where C_v^{nl} is the coefficient for nonlinear receptivity. Here, A_{rs} is the amplitude of the $(0, 2\beta_0)$-mode. The nonlinear receptivity mechanism is most efficient for the lowest frequency ($F = 64$), and the coefficient decreases nearly linearly with increasing frequency. At $F = 64$, there is also a strong linear receptivity mechanism at work, producing unsteady Görtler modes (figure 15a). In contrast, linear receptivity is irrelevant for $F \geqslant 128$ as there exist no unstable travelling Görtler modes. Therefore, the nonlinear mechanism is expected to be particularly relevant at high frequencies.

Grid	R^* (m)	Φ(deg.)	$L_z^*(\times 10^{-2})$ (m)
H	1.0	90.0	8.92
I	4.0	22.5	8.92
J	Flat plate		8.92

TABLE 3. Parameters of the FV meshes. R^* and Φ according to figure 1(*a*). The number of grid points in the tangential, wall-normal and spanwise directions is $1025 \times 129 \times 129$ for all meshes; the total number of points is about 17 million. This corresponds to tangential, wall-normal and spanwise resolutions of $\Delta\xi^+ \times \Delta\eta_w^+ \times \Delta z^+ = 15.7 \times 0.7 \times 7.1$ in viscous units at the inflow where $\Delta\eta_w^+$ is the normal spacing at the wall.

We have demonstrated that steady Görtler rolls can be triggered by free-stream vortical modes both via a linear and a nonlinear receptivity mechanism. Here, we aim to determine a threshold, above which the steady modes are most likely excited by the nonlinear mechanism. This threshold is found by evaluating

$$C_v^{nl} \varepsilon_{v,thres}^2 |_F = C_v \varepsilon_{v,thres}, \qquad (2.14)$$

C_v and C_v^{nl} – the linear and nonlinear receptivity coefficients of the $(0, 2\beta_0)$-mode – are extracted from figures 13(*a*) and 15(*d*), respectively. Note that the threshold depends on the frequency of the oblique-mode forcing. Considering $F = 64$ (128, 256, 384) and steady Görtler rolls with wavelength $\Lambda = 273$, we find $\varepsilon_{v,thres} = 7.9 \times 10^{-2}$ (8.2×10^{-2}, 8.8×10^{-2}, 9.5×10^{-2}). These values are fairly large, suggesting that steady Görtler rolls are more efficiently excited by linear receptivity to steady vortical inflow disturbances than by nonlinear receptivity to pairs of unsteady free-stream modes. However, as discussed above, the linear mechanism is at work only at zero and low frequencies of the free-stream disturbance, whereas the receptivity in the high-frequency range is exclusively due to the nonlinear mechanism. Which of the two receptivity mechanisms would then dominate in a perturbation environment with a broad frequency spectrum such as free-stream turbulence? This issue will be addressed in §3.3.4.

3. Transition due to free-stream turbulence

3.1. *Finite volume code and domain*

Direct numerical simulations of laminar–turbulent transition in Görtler flow with free-stream turbulence were performed using a finite volume (FV) algorithm. The incompressible Navier–Stokes equations are discretized using a local volume flux formulation on a staggered grid (Rosenfeld, Kwak & Vinokur 1991). The convective terms are advanced in time by a second-order Adams–Bashforth method. The pressure and diffusion terms are treated implicitly, using the Euler and the Crank–Nicolson schemes, respectively. The numerical method was validated and verified in previous simulations of transition to turbulence in boundary layers, where the amplification of streaks and their secondary instability must be accurately predicted (e.g. Zaki & Durbin 2005, 2006). It was also applied in transition studies in turbo-machinery geometries where curvature effects can be important (Wu & Durbin 2001; Zaki *et al.* 2010). Table 3 lists the computational meshes used. The physical domain is resolved by $1025 \times 129 \times 129$ grid points in the tangential, wall-normal and spanwise directions, respectively, which amounts to 17 million points in total. The streamwise resolution and the wall-normal stretching of the grid are based on the recommendations by

Jacobs & Durbin (2001) for simulations of bypass transition on flat plates. We verified the spanwise size and resolution by doubling the span and the number of spanwise points and found converged results for the values given in table 3. The grids denoted by H and I are employed for simulations with concave plates of radius $R^* = 1$ and 4 m, respectively. Case J is a comparative simulation with a flat wall, included here to highlight the effect of wall curvature on the transition location. The wall-normal size of the inflow plane of the FV meshes corresponds to that of the SEM grids. The spanwise width and resolution are significantly larger in order to capture a wide range of disturbance length scales within the computational domain.

3.2. *Initial flow field and free-stream turbulence*

The initial conditions were obtained by interpolating the base flows from the SEM simulations onto the meshes for the FV code. The boundary conditions partly differ from those described in § 2.2. The top boundary is shaped so as to include the Blasius displacement thickness $\delta^\star(\xi)$, and a zero-stress condition is prescribed. Convective outflow conditions are used in order to cope with a fully turbulent outflow.

The oncoming free-stream turbulence is prescribed as an inflow condition fluctuating in space and time. It is synthesized by a sum of modes,

$$\boldsymbol{u}_{in}(\eta, z, t) = \sum_{\gamma} \sum_{\beta} \sum_{\omega} \hat{\boldsymbol{u}}(\eta; \gamma, \beta, \omega)\, \mathrm{e}^{\mathrm{i}(\beta z - \omega t)}, \tag{3.1}$$

where ω is the angular frequency and γ and β are the wall-normal and spanwise wavenumbers, respectively. The streamwise dependence $\alpha\xi$, with α being the streamwise wavenumber, has been replaced via Taylor's hypothesis by the time dependence $-\omega t$, assuming a phase speed $c = U_\infty = 1$ of the free-stream waves. The modal coefficients $\hat{\boldsymbol{u}} \equiv (\hat{u}, \hat{v}, \hat{w})$ consist of the streamwise, wall-normal and spanwise components,

$$\left.\begin{aligned}
\hat{u} &= -\frac{1}{\sqrt{\omega^2 + \beta^2}} \left(\frac{\mathrm{i}\omega}{\kappa} A \Phi'_{OS} - \beta B \Phi_{SQ} \right), \\
\hat{v} &= -\frac{\sqrt{\omega^2 + \beta^2}}{\kappa} A \Phi_{OS}, \\
\hat{w} &= -\frac{1}{\sqrt{\omega^2 + \beta^2}} \left(\frac{\mathrm{i}\beta}{\kappa} A \Phi'_{OS} + \omega B \Phi_{SQ} \right),
\end{aligned}\right\} \tag{3.2}$$

where $\kappa \equiv \sqrt{\omega^2 + \gamma^2 + \beta^2}$ is the magnitude of the wavevectors included; Φ_{OS} stands for the Orr–Sommerfeld continuous-spectrum eigenfunctions, computed as described in § 2.3.2, and Φ'_{OS} denotes the wall-normal derivative of Φ_{OS}. The inflow turbulence also contains modes from the continuous eigenvalue spectrum of the Squire equation, denoted by Φ_{SQ}. These are computed in a similar way as the Orr–Sommerfeld free-stream modes (Jacobs & Durbin 1998). Since the Orr–Sommerfeld and Squire continuous-spectrum modes incorporate the presence of the wall, they are a suitable basis to synthesize inflow turbulence downstream of the leading edge of the plate. The coefficients A and B in (3.2), given in Jacobs & Durbin (1998), contain uniformly distributed random angles and are weighted according to the von Kármán energy spectrum of homogeneous isotropic turbulence,

$$E_0(\kappa) \propto \frac{(\kappa L)^4}{[1 + (\kappa L)^2]^{17/6}}, \tag{3.3}$$

Case	γ-range ($\times 10^{-2}$)	β-range ($\times 10^{-2}$)	ω-range ($\times 10^{-2}$)	F-range	f-range (Hz)
FST1	6.5–103.9	7.4–117.6	7.0–112.3	353.9–5662.8	30.5–488.0
FST2	6.5–103.9	7.4–117.6	1.4–22.5	70.8–1132.6	6.1–97.6
FST3	6.5–103.9	7.4–117.6	0.5–7.5	23.6–377.5	2.0–32.5

TABLE 4. Wavenumbers and frequencies of three different fields of free-stream turbulence. The wavenumber and frequency ranges given include 16 modes each. The dimensional frequencies in the last column are based on the experimental reference of Tandiono *et al.* (2008).

where L is the turbulent integral length scale. The specific shape of E_0 and the definition of L can also be found in Jacobs & Durbin (2001). The strength of the free-stream turbulence is set by the turbulent intensity Tu. The energy $E(\kappa)$ of wavenumber κ is

$$E(\kappa) = Tu^2 E_0(\kappa), \tag{3.4}$$

where E_0 is normalized such that $\int_0^\infty E_0(\kappa)\,\mathrm{d}\kappa = 3/2$ and Tu is made dimensionless by U_∞. Here, we consider two values of the turbulent intensity, $Tu = 0.1\,\%$ and $Tu = 1\,\%$, while keeping the integral length scale constant ($L = 5.13\delta_0^\star$).

The free-stream turbulence is isotropic only if the same values of ω, γ and β (in the present reference system) are included in (3.1). The lowest wavenumbers γ and β are determined by the size of the inflow plane, and hence this also sets a lower bound ω_{low} on the frequency. The turbulence field 'FST1' listed in table 4 includes similar ranges of ω, γ and β, i.e. it represents a quasi-isotropic turbulent field. For the other two cases ('FST2' and 'FST3'), we relax the requirement of isotropy and also include frequencies $\omega < \omega_{low}$. This avoids prohibitively large computational domains. The resulting turbulence is nearly isotopic only in cross-stream planes and can be thought of as a field of low-frequency streamwise-elongated flow structures. In the following, we use the frequency parameter F rather than the angular frequency ω. Table 4 also lists the corresponding dimensional frequencies pertaining to the experimental settings of Tandiono *et al.* (2008, case 1).

3.3. *Results*

3.3.1. *Boundary-layer response to free-stream turbulence*

Görtler flow with free-stream turbulence is considered. The wall radius is $R^* = 1\,\mathrm{m}$, and the turbulent inflow 'FST1' (see table 4) is used. This field represents homogeneous quasi-isotropic free-stream turbulence and shall serve as a reference case here. The turbulent intensity is $Tu = 1\,\%$ and the integral length scale is $L = 5.13\delta_0^\star$. Figure 16 shows iso-surfaces of negative and positive streamwise disturbance velocities and of the λ_2 vortex identification criterion. Very long streamwise vortices and low- and high-speed streamwise-velocity streaks with fixed spanwise scales are identified, similar to those seen in figure 5. This suggests that the present free-stream turbulence mainly generates steady Görtler modes. Figure 16 also shows that the primary disturbances soon become susceptive to secondary instabilities in the form of small-scale vortices on the low-speed streaks. The onset of these secondary vortices is strongly spanwise-dependent, as was also noticed by Swearingen & Blackwelder (1987). The secondary instabilities lead to a rapid breakdown of the primary disturbances into smaller scales.

Figure 17 shows contours of constant instantaneous streamwise velocities in various cross-stream planes extracted from figure 16. The cross-sections in figure 17(*a–e*) are at
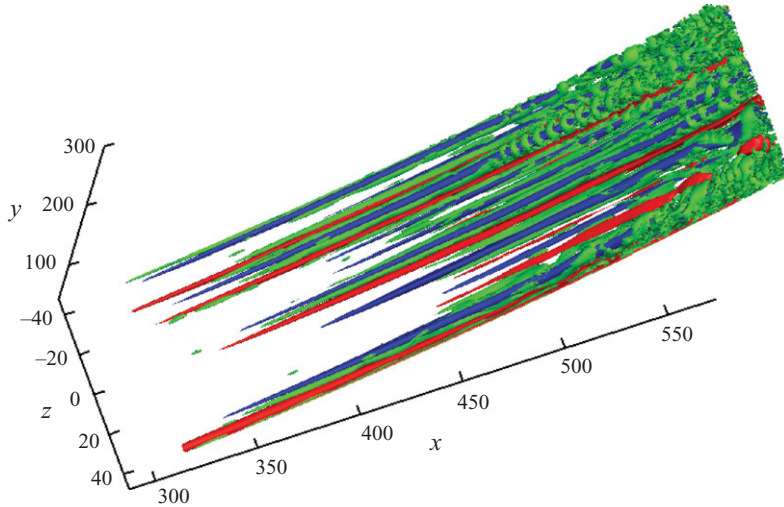
FIGURE 16. Disturbance structures in the transitional region of a Görtler boundary layer ($R^* = 1\,\mathrm{m}$) subjected to free-stream turbulence (field FST1, see table 4; $Tu = 1\,\%$, $L = 5.13\delta_0^\star$). Iso-surfaces of the streamwise disturbance velocity (blue, $u = -0.25$; red, $u = 0.2$) and of the λ_2 vortex criterion (green, $\lambda_2 = -5 \times 10^{-4}$).

the same streamwise positions as those of figure 2(a–e) in Tandiono *et al.* (2008), and we also show the same image sections. From top to bottom, the spanwise variations of the streamwise velocity become more and more pronounced due to the presence of amplifying boundary-layer streaks. These streaks are fixed in the spanwise direction (figure 17a–d), i.e. the dominant primary instabilities are stationary. The low-speed streaks in figure 17(d) feature the characteristic mushroom shape already seen in figure 5(c). One single mushroom structure is seen to emerge from the two low-speed streaks marked by the arrows in figures 17(b) and 17(c). This merging of streaks during the nonlinear stage was also observed in the experiments by Mitsudharmadi, Winoto & Shah (2005). The mushrooms to the left of figure 17(e) have already broken down to smaller scales, whereas the midspan structures are still intact. This illustrates the local nature of the streak breakdown. Far downstream, the primary modes have vanished (figure 17f), and a small-scale irregular pattern is seen.

The visualizations in figure 17 are in reasonable agreement with those of Tandiono *et al.* (2008). However, the flow structures in Tandiono *et al.* (2008, figure 2a–c) are more distinct and 'cleaner' than those shown here. Tandiono *et al.* (2008) used an array of thin vertical wires in order to excite one single Görtler mode with a fixed wavelength. In contrast, we consider broadband free-stream turbulence and hence obtain various Görtler modes with different spanwise scales. The average spanwise wavelength in our simulation is estimated as $\Lambda = 273$, which is close to the value of $\Lambda = 250$ considered by Tandiono *et al.* (2008). The mushroom structures in figures 17(d) and 17(e) indeed feature similar spanwise and wall-normal length scales as those of Tandiono *et al.* (2008, figure 2d, e). However, we observe breakdown of the mushrooms in figure 17(e), in contrast to Tandiono *et al.* (2008). We conjecture that the small-scale free-stream fluctuations required to efficiently trigger the breakdown were absent in the experiments by Tandiono *et al.* (2008).

Figure 18 depicts the prevailing frequencies and spanwise wavenumbers of the boundary-layer disturbance. The same six streamwise locations as in figure 17 are considered. The temporal-spanwise Fourier amplitudes of the streamwise velocity
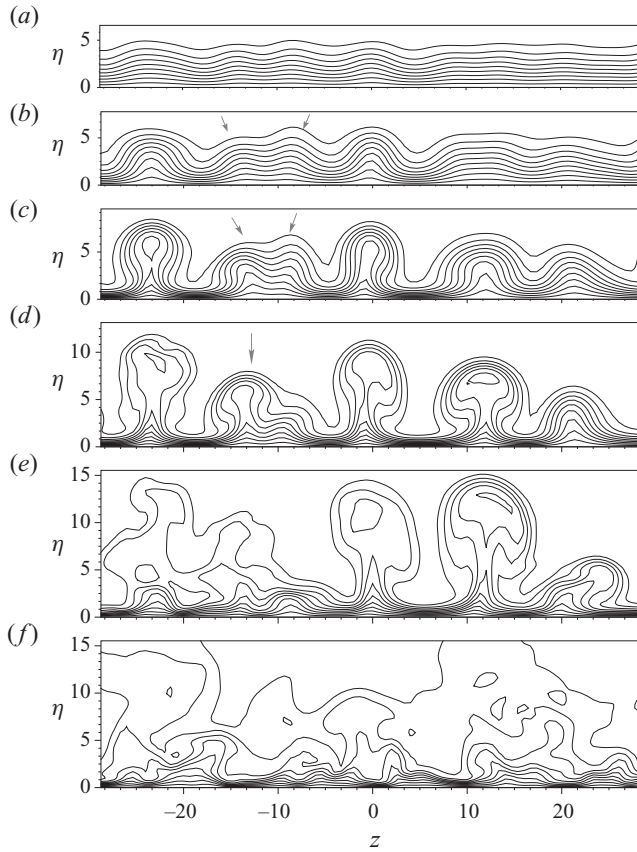
FIGURE 17. Görtler flow ($R^* = 1\,\mathrm{m}$) subjected to free-stream turbulence (field FST1, $Tu = 1\,\%$). Iso-contours of instantaneous streamwise velocity (nine levels $\in [0.1, 0.9]$, spacing: 0.1) at various streamwise positions: (a) $\xi = 280.7$ ($G_\theta = 3.7$), (b) 376.4 (4.5), (c) 472.2 (5.2), (d) 568.0 (5.9), (e) 663.8 (6.5) and (f) 940.4 (8.3). Positions (a–e) and contour levels correspond to those of figure 2 in Tandiono *et al.* (2008); note that only a part of the span of the present domain is shown. The arrows in (b–d) mark the merging of two adjacent low-speed streaks.
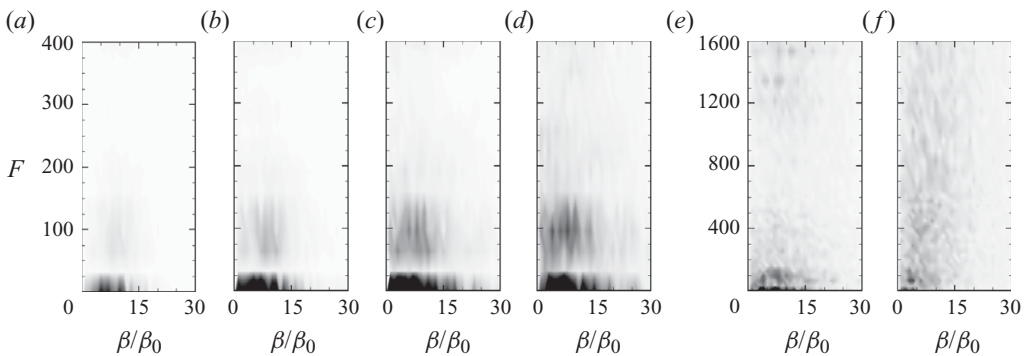

FIGURE 18. Spanwise-wavenumber, frequency spectra in Görtler flow ($R^* = 1\,\mathrm{m}$) subjected to free-stream turbulence (FST1, $Tu = 1\,\%$). Contours of the spanwise-temporal Fourier coefficient $\hat{u}$ of the streamwise velocity (white, $\hat{u} = 0$; black, $\hat{u} \geqslant 0.02$), evaluated at wall-normal location of the maximum total disturbance energy. (a–f) Variation of streamwise location, see caption of figure 17. Note that the range of F in (e) and (f) differs from that in (a–d).
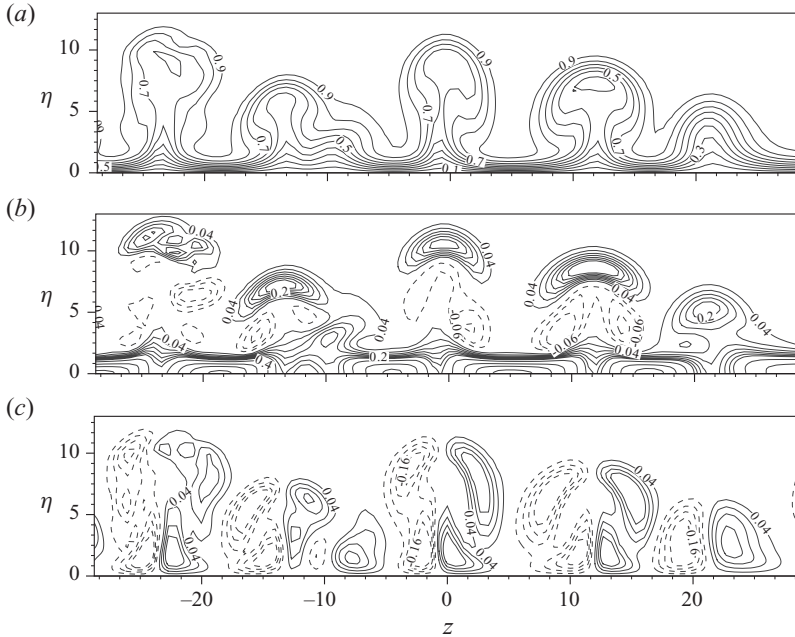
FIGURE 19. Görtler boundary layer ($R^* = 1$ m) subjected to free-stream turbulence (FST1, $Tu = 1\%$). (a) Iso-contours of the streamwise velocity at streamwise position $\xi = 568.0$ ($G_\theta = 5.9$; repetition of figure 17d). (b) Isolines of the wall-normal and (c) spanwise derivative of the streamwise velocity shown in (a). The boundary-layer edge is at $\delta_{99} \approx 12.9$. Compare with figures 5(e) and 6(e) of Tandiono *et al.* (2008).

shown were evaluated at the wall-normal location of maximum total disturbance energy. In the pre-transitional boundary layer (figure 18a–d), the disturbance energy is concentrated on zero or low frequencies. The maximum amplitudes are found for spanwise wavenumbers around $\beta = 7\beta_0$, which yields a dominant wavelength of $\Lambda = 273$. An amplification of unsteady disturbances with frequencies around $F = 96$ is also seen, but these modes are less energetic than the (quasi-)steady contributions. In figure 18(e), we identify weak fluctuations with $F = 1344$ and 1536; a third peak at $F = 3104$ is not shown here. The corresponding dimensional frequencies (based on Tandiono *et al.* 2008, case 1) are $f = 115.8$, 132.4 and 267.5 Hz, respectively. These values are in reasonable agreement with experimental observations and theoretical computations of secondary instabilities and their harmonics. Tandiono *et al.* (2008) detected peaks of $f = 140$, 180 and 280 Hz in their frequency spectra, while Swearingen & Blackwelder (1987) reported a dominant frequency of secondary instability of $f = 130$ Hz. Hall & Horseman (1991) obtained a theoretical value of $f = 110$ Hz for the configuration of Swearingen & Blackwelder (1987). The frequencies and wavenumbers of the primary instabilities are still present in figure 18(e), i.e. not all Görtler modes have broken down to smaller scales yet (intermittent state). The broad frequency spectrum seen in figure 18(f) points to a fully turbulent boundary-layer flow.

3.3.2. *Secondary instabilities and breakdown*

A snapshot of the Görtler flow which undergoes secondary instability is shown in figure 19, in a cross-flow plane. Iso-contours of the instantaneous streamwise velocity are plotted in figure 19(a), and its wall-normal and spanwise gradients are shown in figures 19(b) and 19(c), respectively. The latter two figures highlight regions of intense
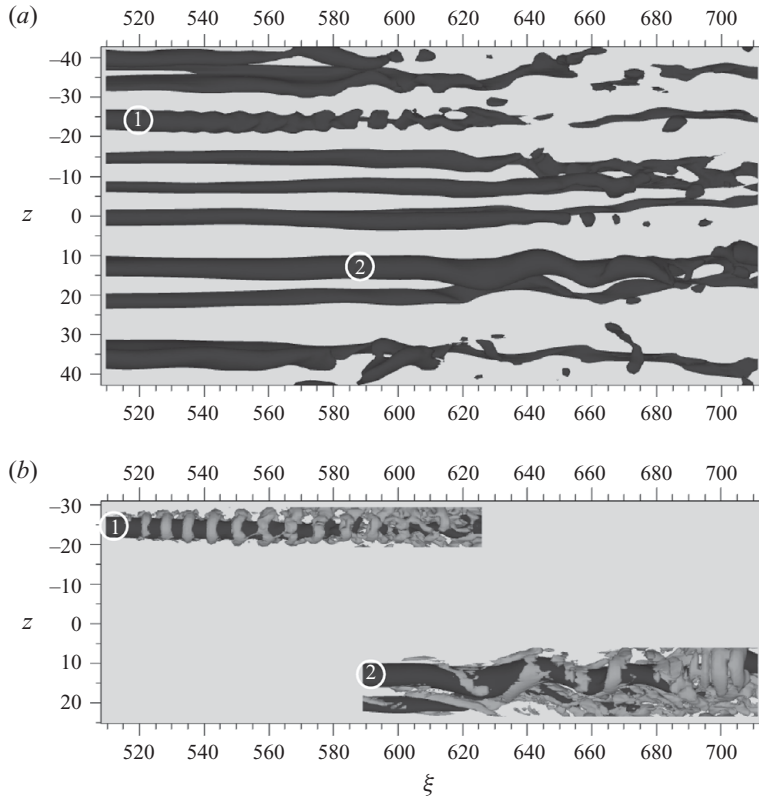
FIGURE 20. (*a*) Low-speed streaks in a Görtler boundary layer ($R^* = 1\,\text{m}$) subjected to free-stream turbulence (FST1, $Tu = 1\,\%$). Iso-surfaces of $u_\xi = -0.2$. (*b*) Vortical structures ($\lambda_2 = -7.5 \times 10^{-4}$, light grey) developing on the streaks labelled by '1' and '2' in (*a*).

wall-normal and spanwise shear and are in good agreement with the results of the reference experiment by Tandiono *et al.* (2008, figures 5*e* and 6*e*). Local maxima of $\partial U/\partial \eta$, indicating wall-normal inflection points of the streamwise velocity profiles, are found at the heads of the mushroom structures near the boundary-layer edge ($\delta_{99} \approx 12.9$); local extrema of $\partial U/\partial z$, marking spanwise inflection points, are seen at the flanks of the mushrooms. Swearingen & Blackwelder (1987) demonstrated that these inflection points are the origins of two types of secondary instability, known as varicose (even) and sinuous (odd) modes. These secondary modes were shown to destabilize the saturated low-speed Görtler streaks (the mushrooms). In figure 20(*a*), we indeed identify two different forms of secondary streak motions – a spanwise symmetric motion and a spanwise anti-symmetric meandering. The streamwise wavelengths of these motions are approximately $\lambda_\xi = 8$ and 33, respectively. This yields a ratio between λ_ξ and the mean spanwise wavelength of the underlying Görtler rolls of 0.7 for the symmetric mode and 2.7 for the anti-symmetric mode. The corresponding ratios obtained from the smoke visualizations of Swearingen & Blackwelder (1987, figure 14*a,c*) are 0.8 for the symmetric oscillation and 1.8 for the meandering. Figure 20(*b*) highlights typical vortex structures accompanying the secondary streak motions. The two numbered streaks of figure 20(*a*) are considered. The first streak undergoes a symmetric oscillation, which becomes manifest as a train of horseshoe vortices. The meandering of the second streak is accompanied by

streamwise-aligned vortices at the flanks of the streaks. Sinuous streak meandering and varicose horseshoe vortices can also occur in combination, as noticed by Swearingen & Blackwelder (1987, figure 14b). The dominant secondary instability in the experiments of Swearingen & Blackwelder (1987) was, though, a purely sinuous mode – owing to its larger growth rate in comparison to the varicose type (Liu & Domaradzki 1993; Yu & Liu 1994). However, the sinuous instability does not generally dominate over the varicose mode. Instead, the type of dominant instability depends on the spanwise wavenumber of the underlying Görtler vortex-streak system. Li & Malik (1995) demonstrated by inviscid secondary-instability analysis that the prevailing instability is of varicose type, if the primary Görtler rolls feature twice the spanwise wavelength of those in Swearingen & Blackwelder (1987). This finding was experimentally confirmed by Asai, Minagawa & Nishioka (2002).

3.3.3. *Temporal-spanwise averages*

The following results were obtained by averaging the flow in the spanwise direction and time. Note that the nonlinear mean-flow distortion is included in the mean. Figure 21(a) depicts the streamwise evolution of the Görtler number for plates with radii $R^* = 1$ and 4 m. Two turbulent intensities are considered, $Tu = 0.1\%$ and 1%, and the Görtler numbers of the laminar reference states are also shown. Transition to turbulence becomes manifest in an increase of the Görtler numbers beyond their laminar counterparts. Figure 21(b) shows wall-normal mean profiles of the streamwise velocity at six downstream positions. At $\xi = 587$, the profile is highly inflectional due to the action of the Görtler streaks. Farther downstream, typical turbulent boundary-layer profiles are seen. The shape factor and the wall-friction coefficient of the boundary layer (figure 21c, d) give a good indication of the transition region. Note that the upstream deviance of the shape factor from the Blasius value is due to a limited accuracy of the calculation of $H_{\delta\theta}$ in the thin boundary layer near the inlet. As expected, the transition zone is located farther downstream when the turbulence intensity is reduced and the wall radius is increased; in the latter case the transitional region also becomes longer. Although the skin friction follows the Blasius distribution in the laminar region of the Görtler boundary layer, its level after transition exceeds that of a turbulent flat-plate boundary layer (by approximately 20%). This behaviour was also observed by Tandiono *et al.* (2009), whose experimental findings are reproduced in figure 21(d). The turbulent skin friction reported by Schultz & Volino (2003) for a strongly curved Görtler boundary layer exceeded the flat-plate value by as much as 40%. Girgis & Liu (2006) proposed the nonlinear modification of the steady Görtler modes by wavy (sinuous) secondary instabilities as a possible mechanism of the large skin-friction rise during transition. Figures 21(c) and 21(d) also indicate that the flat-plate boundary layer – included for comparison – does not transition to turbulence at all, which highlights the dramatic effect of wall curvature.

Figure 21(e) shows that the streamwise boundary-layer disturbance velocity amplifies more rapidly when the wall radius is decreased and the turbulent intensity is increased. All curves exhibit a significant overshoot beyond the level of fully turbulent Görtler flow. This behaviour was also observed in flat-plate boundary-layer experiments with grid turbulence (Fransson, Matsubara & Alfredsson 2005, figure 10a). Using a logarithmic ordinate (figure 21f) reveals a long region of exponential amplification in the case of $Tu = 0.1\%$. The disturbance growth matches that of the steady Görtler mode with spanwise wavelength $\Lambda = 273$, which is the dominant disturbance scale (cf. §3.3.1). For a turbulent intensity of $Tu = 1\%$, the
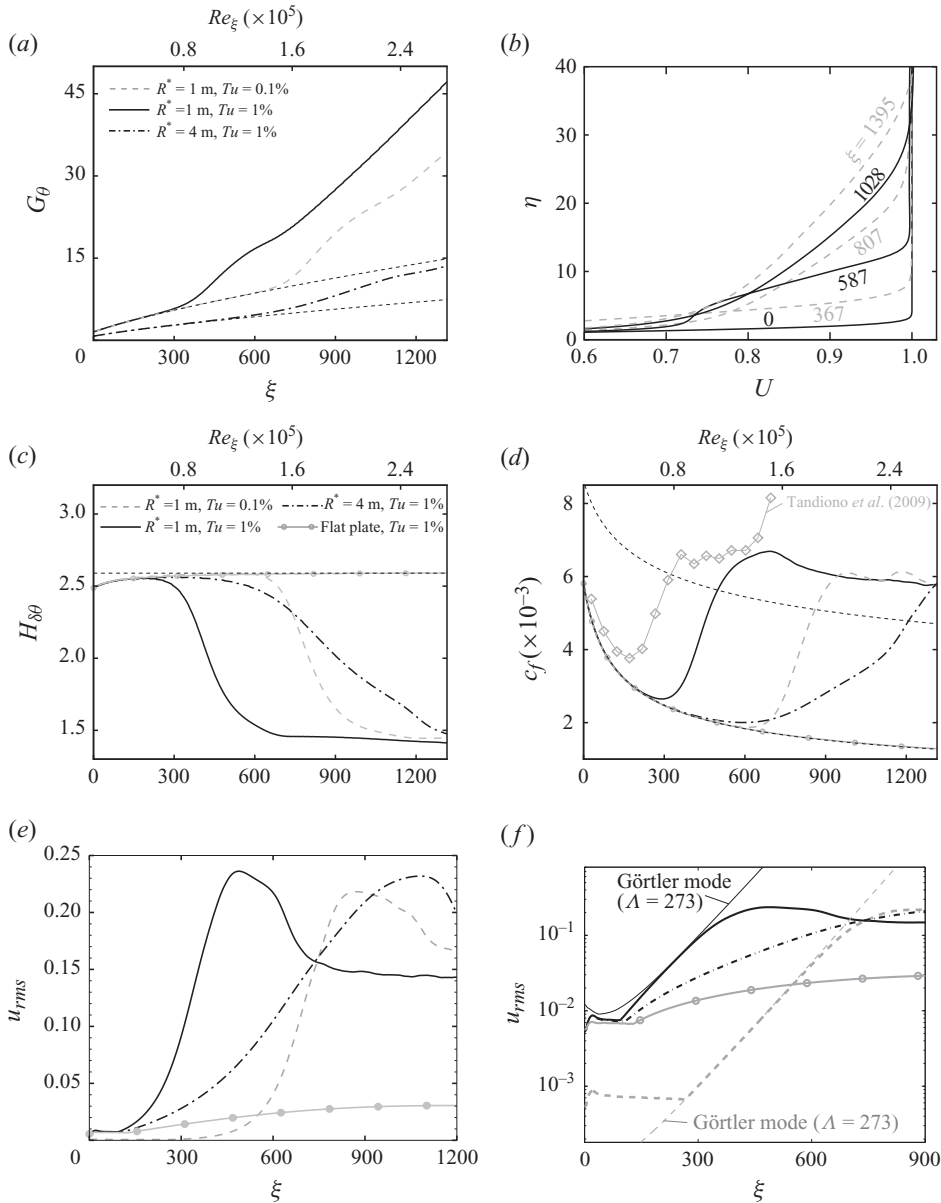
FIGURE 21. Görtler flow exposed to free-stream turbulence (FST1). (*a*) Local Görtler number for different values of R^* and Tu (see legend); dotted lines represent laminar Görtler numbers for $R^* = 1$ and 4 m. (*b*) Mean profiles (temporal-spanwise average) of the streamwise velocity at six streamwise positions. (*c*) Shape factor for various R^* and Tu (see legend); dotted line represents Blasius value. (*d*) Skin-friction coefficient; dotted lines denote c_f in laminar and turbulent flat-plate boundary layers. The experimental results by Tandiono *et al.* (2009, case 1) are also shown. (*e*) Effect of R^* and Tu on the downstream evolution of boundary-layer disturbance. (*f*) Logarithmic plot of the curves of (*e*). Thin lines show evolution of the steady Görtler mode with $\Lambda = 273$. Legend in (*c*) also applies to (*d*–*f*).

linear region in the case of $R^* = 1$ m is much shorter, whereas no clear linear regime is seen for $R^* = 4$ m. This is attributed to an earlier onset of nonlinearity and saturation of the primary disturbance.

3.3.4. *Receptivity to free-stream turbulence*

We have demonstrated in §2.5 that the receptivity of Görtler boundary layers to free-stream vortical modes can be linear or nonlinear – depending on the frequency of the forcing. In order to clarify the relevance of these two mechanisms in Görtler flow with free-stream turbulence, we now also consider the turbulent fields FST2 and FST3. These are characterized by lower frequencies of the most energetic turbulent eddies than those of field FST1 (see table 4). We shall focus on the plate with radius $R^* = 1$ m and consider two values of the turbulent intensity, $Tu = 0.1$ % and 1 %. This hence amounts to six different simulations. When the lowest-frequency field FST3 is specified at the inflow, the local Görtler number rises above the laminar level farther upstream than in the presence of fields FST1 and FST2 (figure 22a). This is especially evident for the lower turbulent intensity ($Tu = 0.1$ %). The speed-up of transition due to fields FST2 and FST3 is also manifested in an upstream shift of the shape-factor drop and the skin-friction rise as compared with the case FST1 (figure 22b,c). Transition is seen to terminate farther downstream for field FST2 with $Tu = 1$ % and farther upstream for FST3 with $Tu = 0.1$ %. Moreover, the shape of the c_f-curve in the transitional region differs for the cases FST2 and FST3 from that of case FST1, suggesting that different modes with different receptivity mechanisms contribute to the primary instability. This is also evident in the evolution of the streamwise disturbance (figure 22d,e). In particular, figure 22(e) shows a significant enhancement of upstream transient growth, if the frequency spectrum of the free-stream turbulence is lowered. This explains why the Görtler boundary layer is most receptive to the turbulence field FST3. Large upstream transients are also triggered by turbulence FST2 with an intermediate frequency spectrum, whereas farther downstream, the boundary-layer disturbance develops in a similar way as that due to FST1. Lowering the turbulent frequency spectrum hence causes a change-over from one primary instability type to another and a speed-up of transition. Figure 22(d) shows that the overshoot in u_{rms} also depends on the frequency spectrum of the free-stream turbulence. This can be explained by a different energy distribution among the high-frequency fluctuations, which terminate the growth of the primary disturbances by triggering the breakdown.

Next, we determine the dominant primary modes and their receptivity to FST1, FST2 and FST3 (figures 23a,d; 23b,e and 23c,f). For each case, the downstream evolution of the most energetic steady and unsteady contributions to the boundary-layer disturbance is shown in terms of the streamwise disturbance amplitude (temporal-spanwise Fourier transform). The dominant steady disturbance excited by field FST1 is a Görtler mode with spanwise wavelength $\Lambda = 273$ (figure 23a). The most important unsteady disturbance is a travelling Görtler mode with frequency $F = 64$ and wavelength $\Lambda = 224$, but its amplitude is much lower than that of the steady Görtler mode. When scaling the curves pertaining to $Tu = 0.1$ % such that they match those for $Tu = 1$ % (figure 23d), we find that the steady Görtler mode scales as Tu^2. The underlying receptivity mechanism hence is nonlinear. The amplitude of the travelling Görtler mode is found to be proportional to Tu^3 and is thus ascribed to triad interactions. Being negligible in the present cases, this mode may become important in an environment of very high turbulent intensity (cf. the experiments by Schultz & Volino 2003).

The turbulence FST2 (figure 23b) produces a dominant steady mode with larger spanwise wavelength ($\Lambda = 453$) than that excited by FST1. This highlights the sensitivity of the boundary-layer disturbance to variations of the length and time scales of the free-stream forcing. The wavelength of the most energetic unsteady
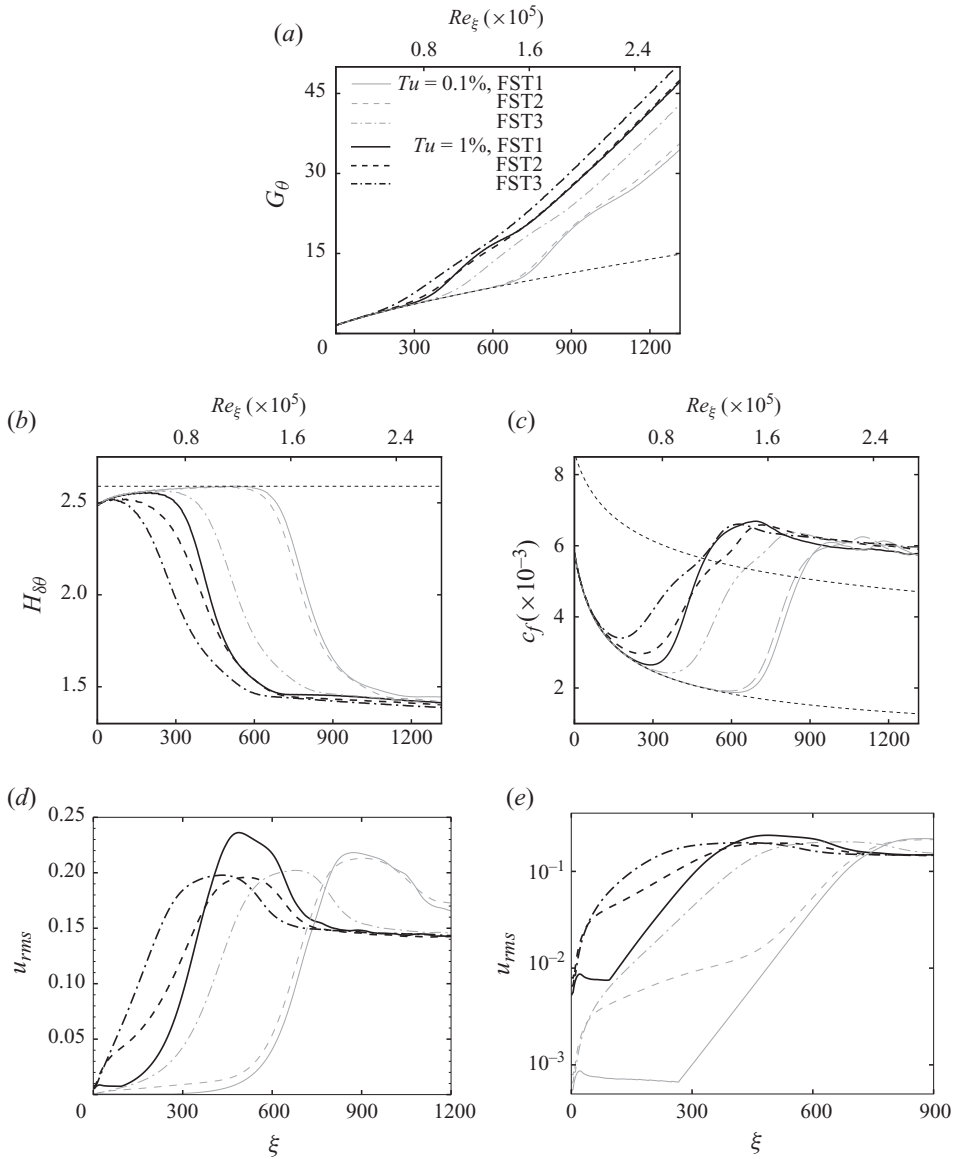
FIGURE 22. Görtler flow ($R^* = 1\,\mathrm{m}$) exposed to the free-stream turbulence of types FST1, FST2 and FST3. (*a*) Local Görtler number for different turbulent fields and intensities (see legend); dotted line: laminar Görtler number. (*b*) Shape factor; dotted line: Blasius value. (*c*) Skin-friction coefficient; dotted lines: c_f in laminar and turbulent flat-plate boundary layer. (*d*) Effect of type of turbulence field and Tu on downstream evolution of the boundary-layer disturbance. (*e*) Logarithmic plot of the curves of (*d*). Legend in (*a*) also applies to (*b*–*e*).

mode is also $\Lambda = 453$, and the frequency is $F = 72$. The transient growth of the unsteady mode is comparable to that of the steady mode. Both modes scale as Tu^2 (figure 23*e*), indicating quadratic receptivity mechanisms. In the case FST3 (figure 23*c*), the prevailing unsteady disturbance ($F = 48$, $\Lambda = 345$) undergoes a larger transient growth than the dominant steady component ($\Lambda = 273$). For $Tu = 0.1\,\%$, the upstream amplitude of the travelling disturbance is significantly larger than that
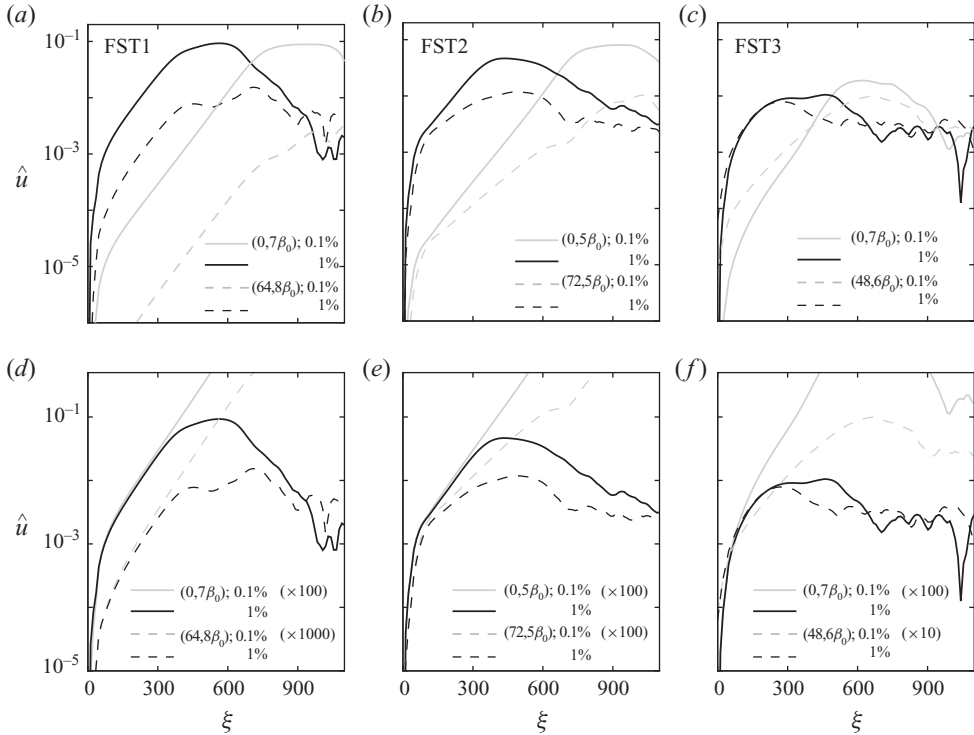
FIGURE 23. Decomposition of the boundary-layer disturbances ($R^* = 1\,\mathrm{m}$) due to free-stream turbulence ($Tu = 0.1\,\%$ and $1\,\%$) into contributions with different frequencies and spanwise wavenumbers (temporal-spanwise Fourier coefficients). The most energetic steady and unsteady modes are shown. (a) Response to turbulence field FST1, (b) FST2 and (c) FST3. In (d–f) the curves of (a–c) pertaining to $Tu = 0.1\,\%$ are scaled to match those for $Tu = 1\,\%$.

of the steady contribution. These strong travelling modes are responsible for the significant upstream shift of transition due to turbulence FST3. The amplitude of the travelling mode is linear in Tu, whereas that of the steady Görtler roll is proportional to Tu^2 (figure 23f). Linear and quadratic receptivity hence coexist in a turbulent environment with low frequencies.

To summarize, the receptivity mechanisms of the model problems with free-stream vortical modes studied in §2.5 were also found in the case of free-stream turbulence. Although the receptivity coefficients of the linear mechanism are larger than those of the nonlinear mechanism, the latter mechanism plays an important role in Görtler flow with free-stream turbulence. The linear mechanism can only generate unsteady Görtler modes with low frequencies and is therefore relevant only if the spectrum of the free-stream turbulence contains enough energy in the low-frequency range. The boundary-layer receptivity to the low-frequency field FST3 is therefore dominated by the linear mechanism and produces travelling Görtler vortices, which enhance transition to turbulence. On the other hand, the receptivity to high-frequency turbulence FST1 is mainly governed by the nonlinear mechanism and leads to steady Görtler rolls. What type of receptivity and instability would then prevail in wind-tunnel experiments with grid turbulence? Kurian & Fransson (2009) investigated the characteristics of various turbulence grids and measured for the coarsest grid (type E) and the lowest free-stream velocity ($2\,\mathrm{m\,s^{-1}}$) a longitudinal integral length scale of $35.8\,\mathrm{mm}$. Using

Taylor's hypothesis, we obtain a frequency of the most energetic turbulent eddies of 56 Hz. Table 4 reveals that field FST1 best represents such kind of grid turbulence. This explains why most experimenters (e.g. Swearingen & Blackwelder 1987) only detected steady Görtler rolls.

4. Conclusions

Boundary-layer flow over concave walls was investigated using spatial DNS. The boundary layer may be destabilized by centrifugal forces owing to the wall curvature, and the dominant instability appears as pairs of steady counter-rotating streamwise vortices, the Görtler rolls. Since alternating positive and negative steady streamwise-velocity streaks, induced by these rolls, are typically observed in experiments, most studies in the literature deal exclusively with steady Görtler instability. However, low-frequency travelling Görtler modes can also attain large amplitudes (see also Boiko *et al.* 2010). To study how Görtler vortices are triggered at the wall and from the free stream, we considered streamwise-localized wall roughness and free-stream vortical disturbances. Roughness was modelled by smooth step-like surface bumps with sinusoidal spanwise shapes, prescribed either as a wall deformation (meshed roughness) or as an inhomogeneous wall boundary condition for the disturbance velocity (linear roughness model). Free-stream vortical disturbances were modelled as an inflow condition consisting of modes from the continuous Orr–Sommerfeld eigenvalue spectrum of Blasius flow. This constitutes a typical receptivity problem which is best described in terms of receptivity coefficients for the instability modes. To our knowledge, the present paper reports the first spatial DNS of Görtler flow used to extract these receptivity coefficients.

The most important results are as follows. The receptivity to wall roughness is linear in the roughness amplitude even for fairly high bumps (40 % of the local displacement thickness). Görtler boundary layers are in particular receptive to roughness elements near the leading edge, while the receptivity decreases significantly farther downstream. Receptivity to roughness also decreases with increasing wall radius. We propose a new scaling of the receptivity coefficient, obtained by normalizing the receptivity amplitude not only by the forcing amplitude but also by the square root of the local Görtler number. This leads to wall-radius independent receptivity coefficients and hence allows a comparison of results obtained on walls with different curvature. We further confirmed that roughness receptivity increases for less localized ('longer') bumps (see e.g. Denier *et al.* 1991). Longer bumps enhance the transient disturbances at the roughness site, which in turn trigger the centrifugal instability and feed the Görtler modes with energy. We also modelled the effect of the roughness by inhomogeneous boundary conditions of the disturbance (linear roughness model) and compared the results with those obtained with meshed roughness. Linear Navier–Stokes computations with the roughness model led to underprediction of the receptivity coefficients by approximately 10 %, while the roughness model performed better in nonlinear simulations. We conclude that solutions to the linearized equations combined with linear roughness models are inaccurate for Görtler boundary layers. A similar conclusion was drawn by Cabal *et al.* (2001) for the case of channel flow with corrugated walls.

Görtler boundary layers are highly receptive to free-stream vortical modes with zero or low frequency, large spanwise wavelength and small wall-normal wavelength. These modes penetrate deeply into the shear, introduce significant streamwise vorticity in the boundary layer and hence efficiently excite boundary-layer streaks by the

lift-up mechanism. These streaks initiate centrifugal instabilities in the form of steady or slowly travelling Görtler vortices. The receptivity mechanism is linear, and is more effective in generating high-amplitude Görtler modes than wall roughness. Görtler boundary layers are also receptive to pairs of high-frequency free-stream vortical waves, producing steady Görtler rolls. The associated receptivity mechanism is quadratic in the amplitude of the free-stream modes. Steady Görtler vortices may thus originate from linear receptivity to steady free-stream vorticity or from nonlinear receptivity to high-frequency fluctuations. The linear mechanism is found to be more efficient than the nonlinear mechanism. In the presence of free-stream turbulence with a broad frequency spectrum, both receptivity mechanisms may act simultaneously to initiate the centrifugal instability, as discussed next.

We present a spatial DNS study of Görtler boundary layers subjected to free-stream turbulence. This type of simulation is reported here for the first time to our knowledge. The free-stream turbulence was modelled by a sum of Orr–Sommerfeld/Squire continuous spectrum modes, and three turbulent fields with different frequency spectra were considered. When high-frequency free-stream fluctuations are prescribed, the dominant primary boundary-layer instabilities are steady Görtler rolls due to nonlinear receptivity. Lowering the frequency range of the turbulence leads to an earlier amplification of the boundary-layer disturbance, which is attributed to travelling Görtler vortices excited by low-frequency free-stream fluctuations (linear receptivity). Under these conditions, linear and nonlinear receptivity (travelling and steady Görtler modes) are competitive. If the turbulent frequency spectrum is low enough, the travelling modes saturate and break down before the steady Görtler rolls, leading to a speed-up of transition to turbulence. However, in the wind-tunnel experiments cited herein, the very-low-frequency free-stream fluctuations required for this scenario were absent or low in energy. This explains why the prevailing primary disturbances in those experiments were steady Görtler modes.

While laminar–turbulent boundary-layer transition in Görtler flow occurs farther upstream than in flat-plate flow subjected to free-stream turbulence, the physical mechanisms of the breakdown to turbulence are similar. The primary disturbances first saturate in amplitude and then develop high-frequency secondary instabilities on the low-speed streaks. We identified two forms of streak instability in our DNS data – a spanwise anti-symmetric meandering and a spanwise symmetric streak oscillation. These modes were also observed in experiments (e.g. Swearingen & Blackwelder 1987) and are known as sinuous and varicose secondary streak instability.

REFERENCES

Asai, M., Minagawa, M. & Nishioka, M. 2002 The instability and breakdown of a near-wall low-speed streak. *J. Fluid Mech.* **455**, 289–314.

Bassom, A. P. & Seddougui, S. O. 1995 Receptivity mechanisms for Görtler vortex modes. *Theor. Comput. Fluid Dyn.* **7**, 317–339.

Berlin, S. & Henningson, D. 1999 A nonlinear mechanism for receptivity of free-stream disturbances. *Phys. Fluids* **11** (12), 3749–3760.

BERTOLOTTI, F. P. 1993 Vortex generation and wave-vortex interaction over a concave plate with roughness and suction. *ICASE Rep.,* pp. 93–101.

BIPPES, H. 1972 Experimentelle Untersuchung des laminar-turbulenten Umschlags an einer parallel angeströmten konkaven Wand. *Heidel. Akad. Wiss., Math.-naturwiss. Kl., Sitzungsber.* **3**, 103–180.

BIPPES, H. & DEYHLE, H. 1992 Das Receptivity-Problem in Grenzschichten mit längswirbelartigen Störungen. *Z. Flugwiss. Weltraumforsch.* **16**, 34–41.

BOIKO, A. V., IVANOV, A. V., KACHANOV, Y. S. & MISCHENKO, D. A. 2010 Steady and unsteady Görtler boundary-layer instability on concave wall. *Eur. J. Mech.* B/*Fluids* **29**, 61–83.

BOTTARO, A. & LUCHINI, P. 1999 Görtler vortices: are they amenable to local eigenvalue analysis? *Eur. J. Mech.* B/*Fluids* **18** (1), 47–65.

BRANDT, L., HENNINGSON, D. S. & PONZIANI, D. 2002 Weakly non-linear analysis of boundary layer receptivity to free-stream disturbances. *Phys. Fluids* **14**, 1426–1441.

BRANDT, L., SCHLATTER, P. & HENNINGSON, D. S. 2004 Transition in boundary layers subject to free-stream turbulence. *J. Fluid Mech.* **517**, 167–198.

CABAL, A., SZUMBARSKI, J. & FLORYAN, J. M. 2001 Numerical simulation of flows over corrugated walls. *Comput. Fluids* **30**, 753–776.

CHEVALIER, M., SCHLATTER, P., LUNDBLADH, A. & HENNINGSON, D. S. 2007 A Pseudo-spectral solver for incompressible boundary layer flows. *Tech. Rep.* TRITA-MEK 2007:07. Royal Institute of Technology (KTH), Department of Mechanics, Stockholm.

COSSU, C., CHOMAZ, J.-M., HUERRE, P. & COSTA, M. 2000 Maximum spatial growth of Görtler vortices. *Flow Turbul. Combust.* **65**, 369–392.

DENIER, J. P., HALL, P. & SEDDOUGUI, S. O. 1991 On the receptivity problem for Görtler vortices: vortex motions induced by wall roughness. *Phil. Trans. R. Soc. Lond.* A **335**, 51–85.

FISCHER, P., KRUSE, J., MULLEN, J., TUFO, H., LOTTES, J. & KERKEMEIER, S. 2008 *NEK5000: Open Source Spectral Element CFD solver*. Available at: https://nek5000.mcs.anl.gov/index.php/MainPage.

FLORYAN, J. M. 1991 On the Görtler instability of boundary layers. *Prog. Aerosp. Sci.* **28** (3), 235–271.

FLORYAN, J. M. & SARIC, W. S. 1982 Stability of Görtler vortices in boundary layers. *AIAA J.* **20** (3), 316–324.

FRANSSON, J. H. M., MATSUBARA, M. & ALFREDSSON, P. H. 2005 Transition induced by free-stream turbulence. *J. Fluid Mech.* **527**, 1–25.

GIRGIS, I. G. & LIU, J. T. C. 2006 Nonlinear mechanics of wavy instability of steady longitudinal vortices and its effect on skin friction rise in boundary layer flow. *Phys. Fluids* **18** (024102).

GÖRTLER, H. 1941 Instabilität laminarer Grenzschichten an konkaven Wänden gegenüber gewissen dreidimensionalen Störungen. *Z. Angew. Math. Mech.* **21**, 250–252.

GROSCH, C. E. & SALWEN, H. 1978 The continuous spectrum of the Orr–Sommerfeld equation. Part 1. The spectrum and the eigenfunctions. *J. Fluid Mech.* **87**, 33–54.

HALL, P. 1982 Taylor–Görtler vortices in fully developed or boundary-layer flows: linear theory. *J. Fluid Mech.* **124**, 475–494.

HALL, P. 1983 The linear development of Görtler vortices in growing boundary layers. *J. Fluid Mech.* **130**, 41–58.

HALL, P. 1990 Görtler vortices in growing boundary layers: the leading-edge receptivity problem, linear growth and the nonlinear breakdown stage. *Mathematika* **37** (74), 151–189.

HALL, P. & HORSEMAN, N. J. 1991 The linear inviscid secondary instability of longitudinal vortex structures in boundary layers. *J. Fluid Mech.* **232**, 357–375.

ITO, A. 1980 The generation and breakdown of longitudinal vortices along a concave wall. *J. Japan. Soc. Aeronaut. Space Sci.* **28**, 327–333 (in Japanese).

JACOBS, R. G. & DURBIN, P. A. 1998 Shear sheltering and continuous spectrum of the Orr–Sommerfeld equation. *Phys. Fluids* **10** (8), 2006–2011.

JACOBS, R. G. & DURBIN, P. A. 2001 Simulations of bypass transition. *J. Fluid Mech.* **428**, 185–212.

KURIAN, T. & FRANSSON, J. H. M. 2009 Grid-generated turbulence revisited. *Fluid Dyn. Res.* **41**, 021403.

LEE, K. & LIU, J. T. C. 1992 On the growth of mushroom-like structures in nonlinear spatially developing Görtler vortex flow. *Phys. Fluids* A **4** (1), 95–103.

LI, F. & MALIK, M. R. 1995 Fundamental and subharmonic secondary instabilities of Görtler vortices. *J. Fluid Mech.* **297**, 77–100.

LIU, W. & DOMARADZKI, J. A. 1993 Direct numerical simulation of transition to turbulence in Görtler flow. *J. Fluid Mech.* **246**, 267–299.

LUCHINI, P. & BOTTARO, A. 1998 Görtler vortices: a backward-in-time approach to the receptivity problem. *J. Fluid Mech.* **363**, 1–23.

MITSUDHARMADI, H., WINOTO, S. H. & SHAH, D. A. 2004 Development of boundary-layer flow in the presence of forced wavelength Görtler vortices. *Phys. Fluids* **16**, 3983–3996.

MITSUDHARMADI, H., WINOTO, S. H. & SHAH, D. A. 2005 Splitting and merging of Görtler vortices. *Phys. Fluids* **17**, 124102.

NG, L. L. & CROUCH, J. D. 1999 Roughness-induced receptivity to crossflow vortices on a swept wing. *Phys. Fluids* **11** (2), 432–438.

PARK, D. S. & HUERRE, P. 1995 Primary and secondary instabilities of the asymptotic suction boundary layer on a curved plate. *J. Fluid Mech.* **283**, 249–272.

PATERA, A. T. 1984 A spectral element method for fluid dynamics: laminar flow in a channel expansion. *J. Comput. Phys.* **54**, 468–488.

PEERHOSSAINI, H. & WESFREID, J. E. 1988 On the inner structure of streamwise Görtler rolls. *Intl J. Heat Fluid Flow* **9** (1), 12–18.

ROSENFELD, M., KWAK, D. & VINOKUR, M. 1991 A fractional step solution method for the unsteady incompressible Navier–Stokes equations in generalized coordinate systems. *J. Comput. Phys.* **94**, 101–137.

SARIC, W. S. 1994 Görtler vortices. *Annu. Rev. Fluid Mech.* **26**, 379–409.

SCHRADER, L.-U., BRANDT, L. & HENNINGSON, D. S. 2009 Receptivity mechanisms in three-dimensional boundary-layer flows. *J. Fluid Mech.* **618**, 209–241.

SCHRADER, L.-U., BRANDT, L., MAVRIPLIS, C. & HENNINGSON, D. S. 2010 Receptivity to free-stream vorticity of flow past a flat plate with elliptic leading edge. *J. Fluid Mech.* **653**, 245–271.

SCHULTZ, M. P. & VOLINO, R. J. 2003 Effects of concave curvature on boundary layer transition under high freestream turbulence conditions. *J. Fluids Engng* **125**, 18–27.

SWEARINGEN, J. D. & BLACKWELDER, R. F. 1983 Parameters controlling the spacing of streamwise vortices on a concave wall. *AIAA Paper* 83-0380.

SWEARINGEN, J. D. & BLACKWELDER, R. F. 1987 The growth and breakdown of streamwise vortices in the presence of a wall. *J. Fluid Mech.* **182**, 255–290.

TANDIONO, S., WINOTO, H. & SHAH, D. A. 2008 On the linear and nonlinear development of Görtler vortices. *Phys. Fluids* **20**, 094103.

TANDIONO, S., WINOTO, H. & SHAH, D. A. 2009 Wall shear stress in Görtler vortex boundary layer flow. *Phys. Fluids* **21**, 084106.

WU, X. & DURBIN, P. A. 2001 Evidence of longitudinal vortices evolved from distorted wakes in a turbine passage. *J. Fluid Mech.* **446**, 199–228.

YU, X. & LIU, J. T. C. 1994 On the mechanism of sinuous and varicose modes in three-dimensional viscous secondary instability of nonlinear Görtler rolls. *Phys. Fluids* **6** (2), 736–750.

ZAKI, T. A. & DURBIN, P. A. 2005 Mode interaction and the bypass route to transition. *J. Fluid Mech.* **531**, 85–111.

ZAKI, T. A. & DURBIN, P. A. 2006 Continuous mode transition and the effects of pressure gradient. *J. Fluid Mech.* **563**, 357–388.

ZAKI, T. A. & SAHA, S. 2009 On shear sheltering and the structure of vortical modes in single- and two-fluid boundary layers. *J. Fluid Mech.* **626**, 111–147.

ZAKI, T. A., WISSINK, J. G., RODI, W. & DURBIN, P. A. 2010 Direct numerical simulations of transition in a compressor cascade: the influence of free-stream turbulence. *J. Fluid Mech.* **665**, 57–98.